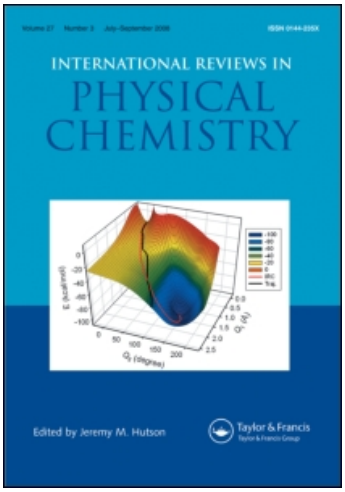

International Reviews in Physical Chemistry
Publication details, including instructions for authors and subscription information:
http://www.informaworld.com/smpp/title~content=t713724383

Electronic structures of graphene edges and nanographene

Toshiaki Enoki[a]; Yousuke Kobayashi[a]; Ken-Ichi Fukui[a]
[a] Department of Chemistry, Tokyo Institute of Technology, Meguro-ku, Tokyo 152-8551

To cite this Article Enoki, Toshiaki , Kobayashi, Yousuke and Fukui, Ken-Ichi(2007) 'Electronic structures of graphene edges and nanographene', International Reviews in Physical Chemistry, 26: 4, 609 — 645
To link to this Article: DOI: 10.1080/01442350701611991
URL: http://dx.doi.org/10.1080/01442350701611991

International Reviews in Physical Chemistry,
Vol. 26, No. 4, October–December 2007, 609–645

Taylor & Francis
Taylor & Francis Group

Electronic structures of graphene edges and nanographene

TOSHIAKI ENOKI*, YOUSUKE KOBAYASHI and KEN-ICHI FUKUI

Department of Chemistry, Tokyo Institute of Technology, W4-1/2-12-1 Ookayama, Meguro-ku, Tokyo 152-8551

(*Received 29 June 2007; in final form 2 August 2007*)

The electronic structure of nanographene having open edges around its circumference crucially depends on its edge shape. The circumference of an arbitrary shaped nanographene sheet is described in terms of a combination of zigzag and armchair edges. According to theoretical suggestions, nanographene has a non-bonding π-electron state (edge state) localized in zigzag edges. This is reminiscent of the non-bonding π -electron state appearing in non-Kekulé-type aromatic molecules. The localized spins of the edge states can give rise to unconventional magnetism in nanographene such as carbon-only ferromagnetism, magnetic switching phenomenon, spin glass state, etc. Nanographene can be prepared by heat-induced conversion of nanodiamond particles. Nanographene ribbons are found by chance around step edges of graphite. The detailed structures of individual nanographene ribbons thus found can be characterized by resonance Raman experiments in which the graphitic G-band is used as a fingerprint. A nanographene sheet inclined along a direction is found to show an interference superperiodic pattern with a varying periodicity. The stacking of sheets also gives an interference effect on the dislocation network created by rhombohedral stacking faults. STM/STS investigations of well defined graphene edges which are hydrogen terminated in ultra-high vacuum condition confirm the presence of edge states around zigzag edges in good agreement with theoretical works. Armchair edges are generally long and defect free whereas zigzag edges tend to be short and defective. This suggests that the armchair edge is energetically more stable than the zigzag edge that has an edge state at the Fermi level. The feature of the edge state depends on the detailed geometry of the edge structures. The edge state in a short zigzag edge embedded between armchair edges becomes less localized due to state mixing with the adjacent armchair edges. The intersheet interaction modifies the spatial distribution of the local density of states of the edge states. The electrons in the edge state in a finite-length zigzag edge are subjected to an electron confinement effect. Nanographene sheets are tailored by cutting along the direction which is chosen intentionally for designing functionality. Well defined edges can be prepared by chemical modifications with foreign atoms or functional groups. A combination of an atomic-resolution electron lithography technique and chemical modifications of the nanographene edges is expected to give nanographene-based molecular devices in the development of nanotechnology. Recent works on the preparations structural and electronic characterizations of graphene edges and nanographene are reviewed.

Contents

*Corresponding author. Email: enoki.t.aa@m.titech.ac.jp

International Reviews in Physical Chemistry
ISSN 0144–235X print/ISSN 1366–591X online
http://www.tandf.co.uk/journals
DOI: 10.1080/01442350701611991

1. Introduction

The discoveries of fullerenes and carbon nanotubes have contributed to enriching the world of carbons, where these newcomers have opened a new realm bridging traditional carbon and nanomaterials [1, 2]. Meanwhile, the sudden prominence of graphene (single sheet graphite) [3–6] in condensed matter physics and electronics applications has recently led us to recognize the importance of understanding graphite as a fundamental issue in nanoscience and cutting-edge device applications in nanotechnology. Indeed, current works [3–12] clarify unconventional electronic features of graphene, which obey the Dirac equation with linear wavenumber dependence. Interestingly, the feature of massless Dirac electrons has been successfully found using a single layer or few-layer graphene prepared merely by cleaving bulk graphite flakes [4, 5]. In addition, these have provided us with new basic issues of condensed matter physics such as an unusual half-integer quantum Hall effect [3, 6, 9], quantum spin Hall effect [7], quantum dots [12], etc.

Fullerenes, carbon nanotubes and graphene are categorized in nanocarbon-based π-electron systems, which are distinguished from sp^3-based nanocarbon systems having a tetrahedral network such as nanodiamond. Nanographene which we discuss in this review is also involved in the family of nanocarbon-based π-electron systems and has features essentially different from those of others. Actually nanographene, which is a nano-sized flat hexagon network, is featured with the presence of open edges around its periphery, in contrast to the absence of edges in ball-shaped fullerenes and an infinite network of graphene, or the negligible contribution of edges in cylinder-shaped carbon nanotubes.

The presence of open edges gives nanographene electronic features entirely different from those of other members in the family of nanocarbon-based π-electron systems. The circumference of an arbitrary shaped nanographene sheet is described in terms of a combination of zigzag and armchair edges, which correspond to *trans*- and *cis*-polyacetylenes, respectively, as shown in figures 1(b) and (c). The electronic

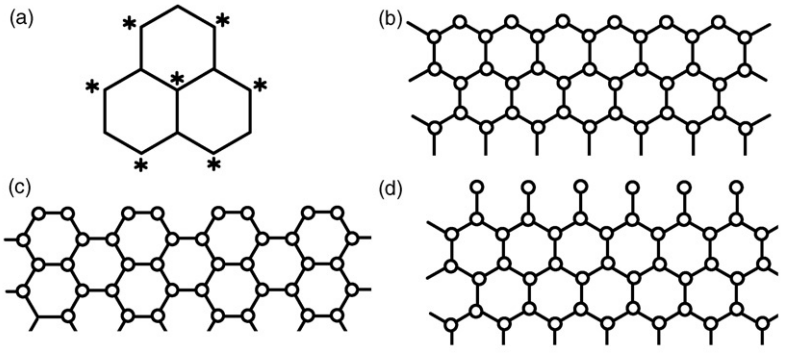

Figure 1. (a) Phenalenyl-free radical where up and down spins are placed on starred and unstarred sites, respectively, (b) zigzag edge, (c) armchair edge, and (d) zigzag edge with its all edge-carbon atoms bonded to one additional carbon atom that participates in the π-conjugated system. (b) and (d) are called 'Fujita edge' and 'Klein edge', respectively.

structure of nanographene depends crucially on the geometry of its edge shape. According to theoretical suggestions [13–20], the presence of zigzag edges adds an extra-electronic state to nanographene; that is, edge-inherited non-bonding π-state (edge state) appears which is superposed upon the bonding π- and antibonding π*-states around the Fermi level E_F. The edge states localized around the zigzag edge region have localized spins, which behave cooperatively with each other forming a magnetically ordered state or a collective state with strong exchange interactions. Therefore, from the magnetism aspects, the localized spins created in the edge states bring about unconventional carbon-only magnetism having features different from traditional magnets. Indeed, recent theoretical works suggest the appearance of ferromagnetism, which varies depending on the structures of nanographene edges [21–24]. For example, a strong ferromagnetic state in which spin polarization is uniformly distributed in space is predicted in a nanographene ribbon with zigzag edge carbon atoms on the one edge side and the other side being monohydrogenated and dehydrogenated, respectively. The interaction between the edge-state spins and the conduction electrons is also suggested to bring about unusual spin-dependent electron transport [25]. Experimental works have also confirmed unconventional spin magnetism associated with the edge-state spins [26–38], consistent with these theoretical suggestions. Ferromagnetism is created in graphene sheets whose edges are hydrogen-terminated by proton irradiation [30–33], in good agreement with the theory. The edge-state spins are found to form a spin glass state in the disordered network of nanographite domains, through the conduction-π-electron-mediated magnetic interaction [28, 29]. The edge-state spins also give novel magnetic functions which have never been observed in existing magnetic materials. Actually, the physisorption of guest molecules into nanographite-based nanoporous carbon shows an interesting magnetic switching phenomenon which originates from the guest-adsorption-induced mechanical compression of nanographite domains [34–36]. A variation of guest species can control the performance of the magnetic switching effect. Furthermore, the edge-state spins can be used as a probe for detecting host-guest interactions [37, 38]. Using the edge-state spins as a probe, a huge condensation of helium is observed in the nanopores of nanographite-based nanoporous carbons.

For investigating the electronic states of nanographene in relation to its structure, it is necessary to prepare nanographene sheets with well defined edge structures. There have been reports on the preparations of nanographene sheets [8, 39–42]. Using silicon carbide as a substrate, graphene thin films were prepared by deposition method [8] or heat-induced conversion [42]. Heat-induced conversion of nanodiamond particles was applied to prepare a single nanographene sheet on a graphitic substrate [40, 41]. Ribbon-shaped nanographene sheets (nanographene ribbons) are found around step edges of graphite samples by chance [43].

The experimental effort for clarifying the features of the edge states in atomic resolution is crucially important in understanding the relationship between the electronic properties and the edge structures. Several works have been made along this direction using scanning tunnelling microscopy (STM)/scanning tunnelling spectroscopy (STS) experiments in ultra-high vacuum conditions with graphene edges well defined by hydrogen-termination [44, 45]. These experiments clearly and comprehensively revealed a variety of features in the edge states depending on the details of the edge structures, in good agreement with theoretical results. Interestingly, the electron confinement effect of edge states is observed in a short length of zigzag edges embedded between armchair edges. The finiteness of the system brings about interference effects on the electrons of nanographene sheets [46, 47]. The boundary condition in the edge of nanographene gives a superperiodic pattern with a periodicity varying along the direction, along which the sheet is inclined. The intersheet interaction also participates in the interference effect.

In the present review article, recent works on the investigations of the edge-inherent electronic structures of nanographene are comprehensively reviewed. Section 2 is devoted to the theoretical background. The preparation and structural characterizations of nanographene are shown in Section 3. The interference and electron confinement effects are discussed in Section 4. Section 5 deals with the electronic structure of the edge states in relation to the details of the edge structures. The conclusion is given in Section 6.

2. Theoretical basis of the electronic structure of nanographene

Most chemists know that the electronic structure of benzene is described with six π-orbitals, which are split into three occupied bonding π-levels and three unoccupied antibonding π^*-levels located below and above the Fermi level E_F, respectively, with a finite HOMO-LUMO level splitting. Condensed polycyclic aromatic hydrocarbons formed by the fusion of benzene rings also have similar electronic structures with the number of π-orbitals and the HOMO-LUMO level splitting increasing and decreasing, respectively, upon an increase in the number of associated benzene rings. In the limit of an infinite size, a graphene sheet or two-dimensional (2D) graphite has the electronic structure of zero-gap semiconductor featured with bonding π- and antibonding π^*-bands, which touch each other at E_F with no HOMO-LUMO splitting [48]. The group of these condensed polycyclic aromatic hydrocarbons therefore has common electronic properties based on these π-orbitals. However, among these, there is a sub-family of non-Kekulé aromatic molecules which

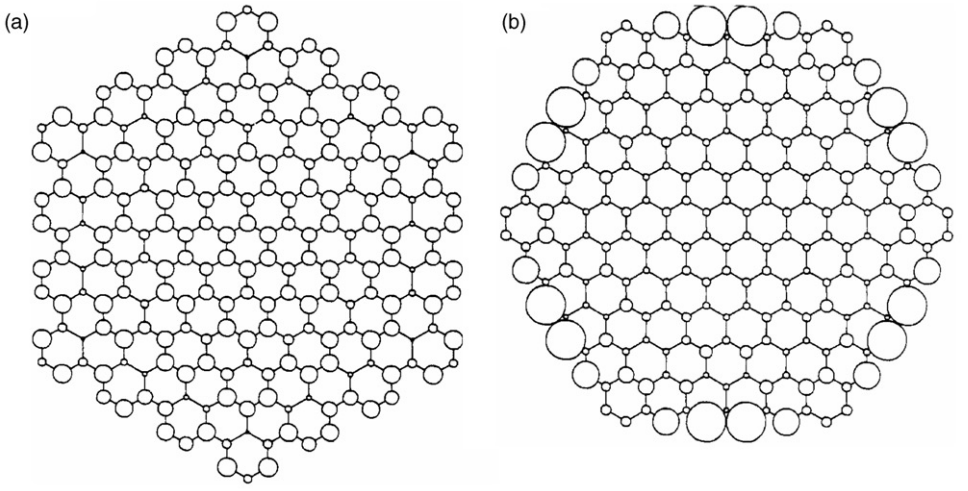

Figure 2. The spatial distribution of the populations of the HOMO level for nanographene sheets with their edges having (a) armchair and (b) zigzag structures [13].

particularly feature magnetism [49, 50]. A typical example is the phenalenyl free radical consisting of three benzene rings fused, in which an unpaired electron having a localized magnetic moment $S = 1/2$ exists as a consequence of the presence of a non-bonding π-electron state at E_F in addition to the π- and π^*-levels as shown in figure 1(a). In general, we can group all the carbon sites of a condensed polycyclic aromatic hydrocarbon molecule into two subgroups, where the neighbouring sites directly bonded to a site belonging a subgroup (subgroup A or starred) belong to another subgroup (subgroup B or unstarred). According to Lieb's theorem [51], unpaired electrons are created when the numbers of sites belonging to these two subgroups are different. Actually, the difference in the numbers between the starred and unstarred sites corresponds to the number of unpaired electrons. In the case of the phenalenyl free radical, the difference gives one localized spin $S = 1/2$. The issue of starred and unstarred sites is the same in a bipartite lattice in the language of physics. A similar idea is also applicable to a nano-sized graphene sheet. It should be noted that the non-bonding state is distributed around the edge of the non-Kekulé molecules [52], similar to the edge state in nanographene.

The circumference of a nanographene sheet having an arbitrary shape can be described in terms of a combination of zigzag edges and armchair edges, which mimic the structures of *trans*- and *cis*-polyacetylenes, respectively, as shown in figures 1(b) and (c). According to theoretical predictions [13–16], zigzag edges give a non-bonding π-electron state (edge state) of edge origin, whose energy level appears at the contact point between the π- and π^*-bands. Figure 2 is an example of the appearance of an edge state localized around the zigzag edge region. It shows the difference in the spatial distributions of the electron populations in nanographene sheets having armchair and zigzag edges [13]. The edge state, which is assigned to the HOMO level in the figure, has populations well localized around the zigzag edge region in the zigzag-edged nanographene sheet (figure 2b), in contrast to uniformly distributed populations of the

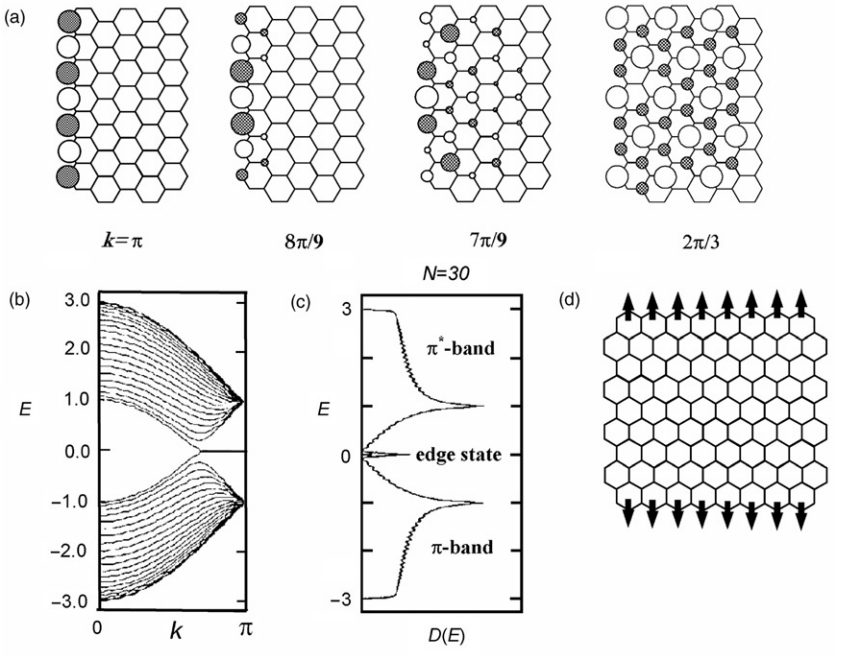

Figure 3. (a) The wavenumber dependence of the populations of the edge state, (b) the energy dispersions of a nanographene ribbon having zigzag edges with a width of 30 unit cells, (c) the density of states, and (d) ferromagnetic spin arrangement at the zigzag edges. All the edge carbon atoms are terminated with hydrogen atoms [15].

HOMO level in the graphene sheet with armchair edges (figure 2a). A large local density of states (LDOS) in the edge region of the zigzag-edged nanographene sheet is confirmed as a non-bonding edge state. Another example is a nanographene ribbon having zigzag edges [15] shown in figure 3. The edge state of the nanographene ribbon is localized around the zigzag edges and appears as a dispersionless state in the wavenumber region from the Brillouin zone edge to $2/3\pi$ of the zone. The edge state, which is completely localized in the Brillouin zone edge, becomes more delocalized as the wavenumber approaches $2/3\pi$, and finally becomes completely delocalized at $2/3\pi$, as shown in figures 3(a) and (b). The edge state is merged to the bonding π- and antibonding π*-bands in the central region $0 \leq k \leq 2/3\pi$. The emergence of an edge state has the same origin as that of the non-bonding state in non-Kekulé-type aromatic molecules. From the language of physics, the edge state originates from the symmetry breaking phenomenon of the Dirac electrons in the boundary condition at zigzag edges [17]. Nanographene sheets with their edges being zigzag are not well stabilized in energy compared with armchair-edged nanographene sheets, since the edge state appears as a half-filled state at the Fermi level [13]. This is reminiscent of the unstable structure of non-Kekulé aromatic molecules having a non-bonding π -state in the energy gap [18, 19], in comparison with Kekulé molecules, in which resonance gives a large HOMO-LUMO separation between the π-bonding and π*-antibonding states.

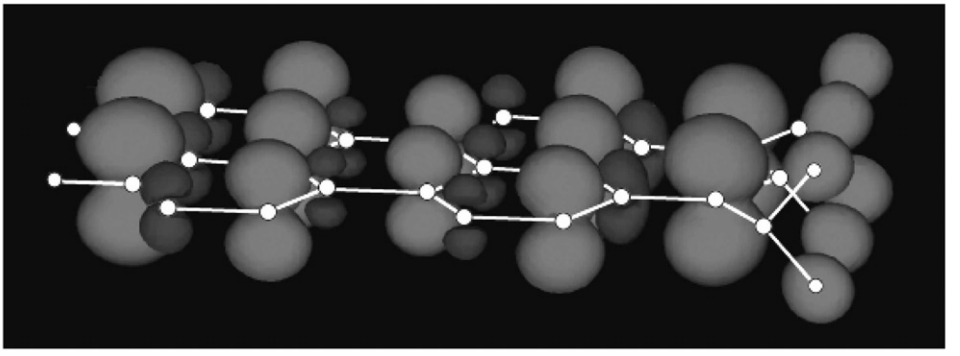

Figure 4. Spin polarization of a zigzag-edged nanographene ribbon where all the edge carbon atoms on one edge side are dihyrogenated with those on the opposite edge side being monohydrogenated. The large light grey circles represent the densities of up-spins, while the small dark grey circles those of down-spins. (Ref. [23], by courtesy of Prof. K. Kusakabe.)

The presence of the edge states, whose density of states has a sharp peak around E_F as shown in figure 3(c), gives rise to localized magnetic moments. Therefore, nanographene is of particular interest from a magnetism viewpoint, where even ferromagnetism happens to be created as exhibited in figure 3(d). Chemical modification of zigzag edges with foreign species is predicted theoretically to give a variation of this magnetism [21–24]. A zigzag-edged nanographene ribbon with all the edge carbon atoms monohydrogenated on both sides of the ribbon has edge states localized at the edges. This corresponds to the case shown in figure 3. A monohydrogenated zigzag edge is called a Fujita edge. When all the edge carbon atoms of the zigzag edge on one side of a zigzag-edged nanographene ribbon are dihydrogenated with those on the opposite side remaining to be monohydrogenated, a completely localized non-bonding state appears around E_F, where all the carbon atoms are spin polarized even in the interior of the nanographene ribbon as shown in figure 4. This is an interesting carbon-only ferromagnetism, in which all the carbon atoms are spin polarized ferromagnetically. The dihydrogenation of the zigzag-edge carbon atoms creates a modified zigzag edge (a Klein edge) [21–24], whose structure is schematically shown as a beard zigzag edge in figure 1(d). In contrast to hydrogenation, fluorination of edges tends to suppress magnetism due to the tendency of forming a closed shell in fluorine [23, 24]. In a zigzag-edged nanogapehene ribbon with one edge side monofluorinated and the opposite side difluorinated, the spin polarization can survive only around the edge region where the edge carbon atoms are monofluorinated. An interesting example is the oxidation of carbon atoms on one zigzag edge side. The monohydrogenated edge works as a magnetic edge while the oxidized edge forms electron conduction paths [23, 24]. This means that the chemical modification can play different roles to these two edges that are chemically modified in different fashions.

These theoretical predictions therefore suggest that we can make a large variety of magnetic nanosystems, which are expected to contribute to developing new types of molecular spintronics/electronics devices on the basis of the magnetism of nanographene.

3. Preparation and structures of nanographene

3.1. *Preparation of a nanographene sheet*

Graphene sheets (a single sheet or a few layer sheet) can be prepared merely by cleaving graphite crystals according to recent experiments [4–6]. Using silicon carbide as a substrate, graphene thin films were prepared by deposition method [8] or heat-induced conversion [42]. However, we need other technique for preparing a nanosized graphene sheet (nanographene). The synthesis of nanographene ribbons grown from a SiC by arc discharge has been reported. The nanographene ribbon thus prepared is bifurcated along the *c* axis, forming a nano-*Y* junction [39]. According to previous work [40, 41], heat-induced conversion of nanodiamond particles can give a single sheet of nanographene. It has already been demonstrated that nanodiamond particles are transformed to graphite by heat-treatment at 1600°C [53, 54]. Accordingly, nanodiamond particles electrophoretically seeded on a substrate can be converted to nanosized graphite without fusion if the inter-nanodiamond-particle distance can be long enough to isolate individual particles from each other by controlling the concentration of the nanoparticles in the controlled electrophoretic condition. Here, we show the preparation of nanographene sheets using the heat-induced conversion of nanodiamond particles.

Isolated nanodiamond particles with a mean size of 5 nm are deposited on a substrate of highly oriented pyrolytic graphite (HOPG) by an electrophoretic technique in which the electrode potential is adjusted to optimize the distribution of nanodiamond particles. The nanodiamond particles seeded on the HOPG substrate are heated at 1600°C in a graphite furnace under argon gas atmosphere for 30 min. The large area STM topography shown in figure 5 reveals the presence of isolated nanographene sheets on the surface of the HOPG substrate. The nanographene sheets have a circular shape with a mean size of ca.10 nm. Figure 6 gives a detailed analysis of one nanographene sheet observed in figure 5(b). The atomically resolved STM picture

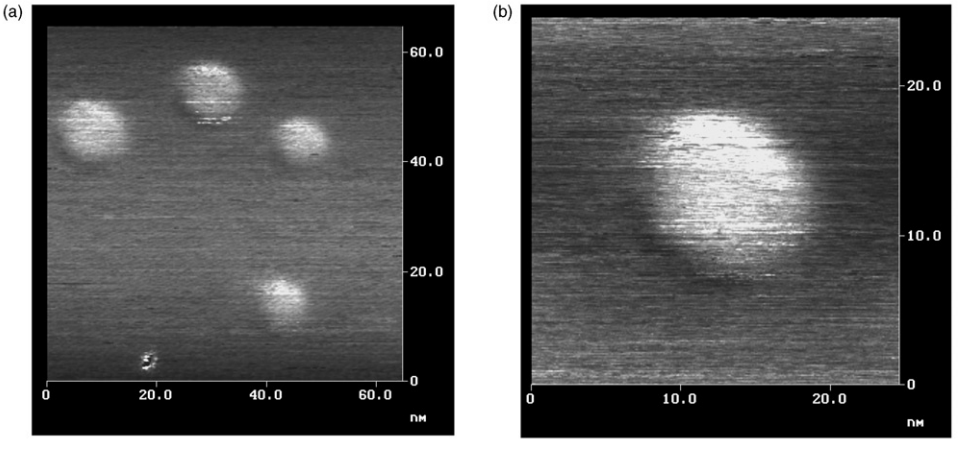

Figure 5. STM images of nanographene sheets obtained after heat-treatment of nanodiamond particles at 1600°C. (b) is a magnified image, whose lattice image is exhibited in figure 6(a) [41].

(figure 6a) obtained from the surface of an isolated nanographene sheet clearly shows a triangular pattern with a lattice constant of 0.25 nm characteristic of the graphite image. The line-profile analysis in figure 6(b) shows that the height of observed particles is in the range of 0.35–0.37 nm in all cases, which is considerably larger than the intersheet distance of 0.3354 nm in bulk graphite. These findings demonstrate the formation of a single sheet of nanographene. The number of carbon atoms involved in this nanographene sheet is roughly estimated at $N \approx 3000$. From the viewpoint of organic chemistry, this is the largest condensed polycyclic aromatic molecule ever having been observed.

Nanodiamond particles when merely heated at 1600°C yield polyhedral nanographite particles with a hollow inside [53, 54]. Therefore, it is surprising to observe a single flat nanographene sheet instead of spherical or polyhedral graphite particles. A trace of oxygen in the argon gas in the graphite furnace might react with the surface of a nanodiamond particle, and consequently a part of the particle is oxidized during the heat-treatment. In the case of the nanodiamond particles deposited on the HOPG

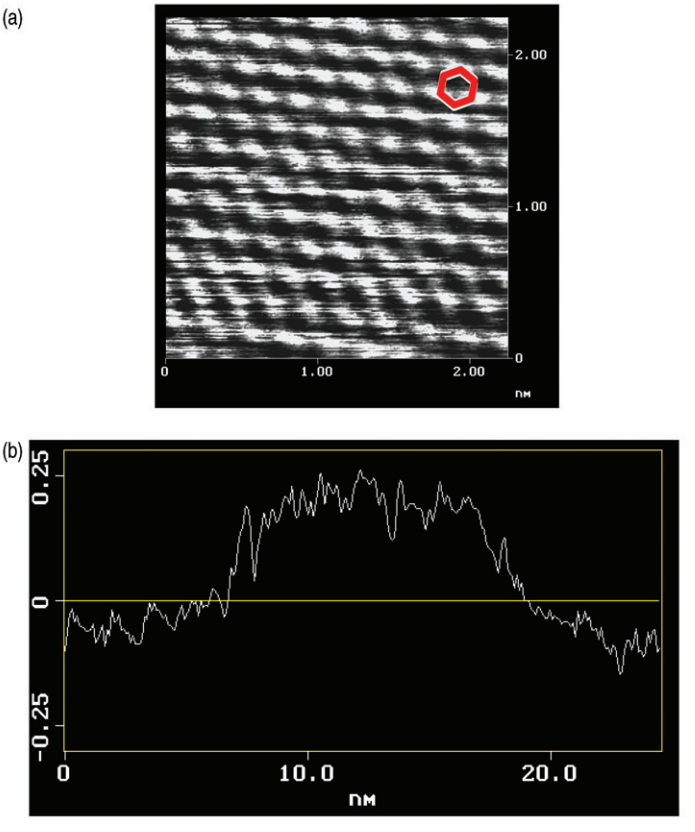

Figure 6. STM lattice image (a) and the line profile (b) of the single sheet of nanographene (figure 5b) on a HOPG substrate. The line profile (b) is in the horizontal direction across the centre of the nanographene sheet. The hexagon in (a) represents a benzene ring [41].

substrate, the surface of the nanodiamond particle in contact with the HOPG surface is more stable against the oxidation compared to the free exposed part. Also, the part in contact with HOPG converts to graphite faster than the free part. The newly converted graphite interacts with the flat HOPG substrate giving rise to the flat nanographene sheets. This results in the formation of single sheets of nanographene. Here we compare the atomic images between the nanographene sheet and the HOPG substrates for characterizing the structural feature in detail. Both images are featured with the triangle superlattice. The in-plane unit cell axes in nanographene sheets are found to be in the same direction as those of the substrate, suggesting that nanographene sheets are placed epitaxially on the substrate. The triangular lattice image is the consequence of the *AB* stacking mode of nanographene sheet with the HOPG substrate. The elongated intersheet distance 0.35–0.37 nm in comparison with that of bulk graphite (0.3354 nm) leads to a weak interaction contributing to the unclear lattice image of the nanographene sheet. From the observed distance between the nanographene sheet and the substrate, the interaction (the interlayer resonance integral γ_1) becomes reduced [55] by 26–50% when the interlayer distance is elongated from the bulk to 0.35–0.37 nm, where $\gamma_1 = 0.39$ eV for bulk graphite [48]. This is a desirable situation for investigating the electronic structure of individual nanographene sheets since it is rather free from the intersheet interaction.

3.2. *Structural characterization of nanographene ribbons*

Nanographene ribbons happen to be found by chance around the step edges of a graphite surface. Next we discuss the structure of nanographene ribbons investigated by a combination of atomic force microscopy (AFM) and resonance Raman experiments of the graphite E_{2g2} mode, which is the signature of the graphitic structure [43]. The Raman peak of the nanographene ribbons exhibits a dependence of its intensity on the light polarization direction relative to the nanographene ribbon axis. This result is due to the quantum confinement of the electrons in the 1D band structure of the nanographene ribbons, combined with the anisotropy of the light absorption in 2D graphite, in agreement with theoretical predictions [56]. We present a polarized Raman study of nanographene ribbons thus found at HOPG step edges. The Raman peaks of the nanographene ribbon and the HOPG are split due to different thermal expansions of the ribbon and the substrate.

Figure 7(a) shows an AFM image, where many ribbons parallel to each other are observed. The average width of the ribbons is 8 nm and the length can be as large as 1 μm. Figure 7(b) shows an AFM image where the presence of a ribbon near a step of the HOPG substrate is evident. The ribbon is larger than 500 nm in length. The height profile (figure 7c) shows a height of 0.35 nm, which corresponds exactly to the interlayer distance of bulk graphite, indicating that the ribbon has only one sheet of atoms. The Raman spectra were taken in the region of the sample where the ribbons depicted in figure 7(a) were observed.

Figure 8(a) shows the Raman spectra obtained with different polarization directions for the incident light with the laser excitation energy of $E_{\text{laser}} = 2.41$ eV. The propagation of the incident light is perpendicular to the graphite plane and θ is the angle between the longitudinal direction of the ribbon and the light polarization ($\vec{P}$)

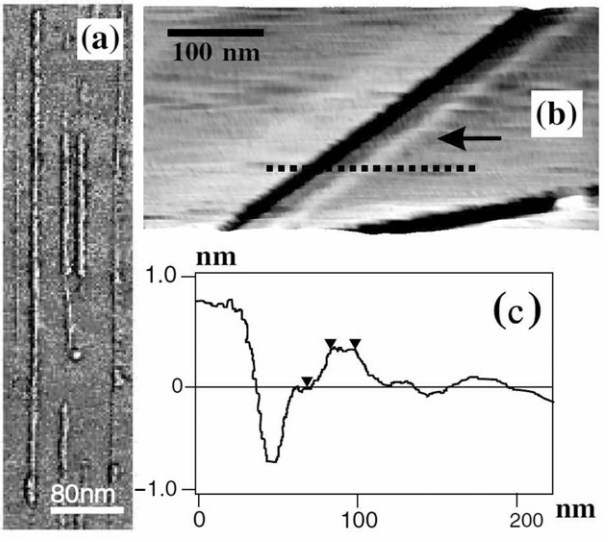

Figure 7. (a) AFM image of many nanographene ribbons parallel to each other. (b) AFM image of a nanographene ribbon near a step edge. The arrow indicates the position of the ribbon for reference. (c) The height profile obtained through the dotted line in (b) [43].

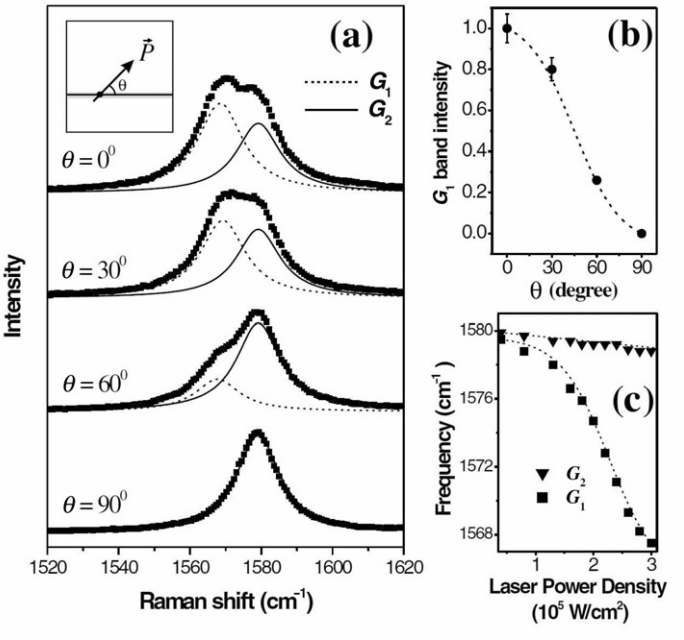

Figure 8. (a) Raman spectra obtained for light incident with different polarization angles (θ) with respect to the nanographene ribbon direction. The inset shows a schematic figure of the sample (horizontal grey line) showing the direction between the ribbon axis and the light polarization vector ($\vec{P}$). (b) Intensity of the G_1 peak versus θ. The dotted line is a $\cos^2\theta$ theoretical curve. (c) Raman frequencies of the G_2 (triangles) and G_1 (squares) peaks as a function of the laser power intensity. The laser energy for the excitation is $E_{\text{laser}} = 2.41$ eV [43].

(inset to figure 8a), where the information about the ribbon direction was obtained by AFM (figure 7a). The observed Raman band is composed of two peaks (G_1 and G_2), centred, respectively, at 1568 and 1579 cm^{-1}. G_2 is assigned to the G-band of the HOPG substrate. G_1 is ascribed to the G-band of a nanographene sheet as we will see next. The intensity of the G_1 peak decreases gradually according to the functional form of a $\cos^2\theta$ curve upon the increase in θ as shown in figure 8(b). The angular dependence of the Raman spectra shown in figures 8(a) and (b) can be explained by considering the selection rules for light absorption in graphite and the quantum confinement in a 1D nanographene ribbon. According to theoretical calculations for 2D graphene, the probability of light absorption $W(\vec{k})$ per unit time is associated with the polarization vector of incident light $\vec{P}= (P_x, P_y)$ and with the wavevector $\vec{k}= (k_x, k_y)$ of the electron by [56]

$$W(\overrightarrow{k}) \propto \frac{|\overrightarrow{P} \times \overrightarrow{k}|^2}{k^2}, \tag{1}$$

where $\vec{k}$ is measured from the K point situated at the corner of the first Brillouin zone. Equation (1) shows that the light absorption has a maximum for electrons with a $\vec{k}$ vector perpendicular to the polarization of the incident light ($\vec{P}$) and is zero for electrons with $\vec{k}$ parallel to $\vec{P}$. This fact is not measurable in 2D crystalline graphite because the density of electrons involved in the absorption process is isotropic in the graphene plane, and no changes in the Raman intensity can be observed by rotating the incident light polarization [56], as confirmed by the absence of the angular dependence in the Raman G_2 peak intensity of the HOPG substrate. In the situation of nanographnene ribbons, the k dependence for the light absorption process is important. The electronic structure of nanographene ribbons is formed by 1D subbands due to the quantization of the k space in the transverse ribbon direction. These 1D subbands are obtained by folding the dispersion curves of 2D graphene along cutting lines [15, 16]. Therefore, the electronic density of states (DOS) exhibits 1D van Hove singularities which depend on the width of a nanographene ribbon [15–17, 57, 58].

Interestingly the Raman signal intensity from a nanographene ribbon is similar to that from the HOPG substrate. This is possible by considering the quantum confinement of the electronic states in the ribbon. The optical absorption process in nanographene ribbons is associated with electronic transitions between the 1D valence π- and conduction π*-subbands [59, 60]. The quantum confinement of the electrons in a 1D structure restricts the wavevectors ($\vec{k}$) of the electrons involved in the absorption process that are associated with transitions between van Hove singularities in the valence and conduction bands. The optical transition energies between van Hove singularities are different for nanographnene ribbons with different widths. By scanning the sample, the Raman signal from a particular nanographene ribbon is obtained when the light spot reaches a ribbon that is in resonance with the energy of the laser beam $E_{laser} = 2.41$ eV. When the photon energy of the incident laser is resonant with an allowed transition between singularities in the 1D density of electronic states, the Raman scattering cross-section diverges, and the intensity of the Raman peak

is enhanced. This resonant mechanism selects the $\vec{k}$ vector of electrons and only those perpendicular to the longitudinal ribbon direction are involved in the absorption process. According to equation (1), we expect that $W(\vec{k}) \propto \cos^2\theta$, since the light absorption probability is proportional to the square of the projection of the polarization vector ($\vec{P}$) in the direction perpendicular to the longitudinal ribbon direction. The experimental results shown in figures 8(a) and (b) are in excellent agreement with theoretical predictions and allow us to conclude that the G_1 peak is indeed associated with the E_{2g2} vibrational mode of the nanographene ribbon.

Here it should be noted that the Raman spectra can distinguish a zigzag-edged nanographene ribbon from an armchair-edged one [43]. An armchair nanographene ribbon gives only the *G*-band. In contrast, a *D*-band, which is not observed in defect-free regular graphene sheet, is expected to appear in a zigzag nanographene ribbon in addition to the presence of a *G*-band. Therefore Raman experiments can be used for characterizing the shape of a nanographene sheet. The experimental characterizations of the edge structure will be a necessary task in the next step.

Finally, it is worth analysing the laser power dependent frequency shift of the G_1 of nanographene depicted in figure 8(c). In fact, this shift is due to a thermal effect. According to figure 8(c), the frequencies of G_1 and G_2 decrease with increasing laser power, owing to the increase in the local temperature. However, the G_1 frequency decreases nonlinearly, whereas the G_2 frequency exhibits only a small laser power dependence. This is expected, since the Raman frequency of nanosized graphene systems exhibits a stronger thermal dependence compared to bulk graphite [61–63]. The high thermal conduction coefficient in the graphene plane avoids the excessive heating with the increase of the laser power density, keeping the lattice parameters almost constant. However, in nano-size systems, the heat dissipation is less efficient, and therefore the force constants are more affected, providing a strong dependence of the Raman frequency on laser power density, as shown in figure 8(c). It is interesting to emphasize that this thermal effect makes possible the observation of a Raman signal from a nanographene ribbon sitting on a graphite bulk substrate.

4. Interference phenomena of electrons on a graphene sheet

The nanosized structures of nanographene sheets are interesting targets for observing interference phenomena in the 2D π-electron systems. In this section, we present examples of the electron confinement effect observed on a nanographene sheet and at the interface between graphene sheets and the substrate.

4.1. *In-plane interference phenomenon and the electron confinement in an inclined nanographene sheet*

The first place is devoted to the interference of the π-electrons confined in a nanographene sheet, which is investigated by the STM technique [46]. In figure 9(a) is shown an STM image of a necktie-shaped nanographene sheet with a size of about 200 nm in width and >400 nm in length. The distance between the nanographene

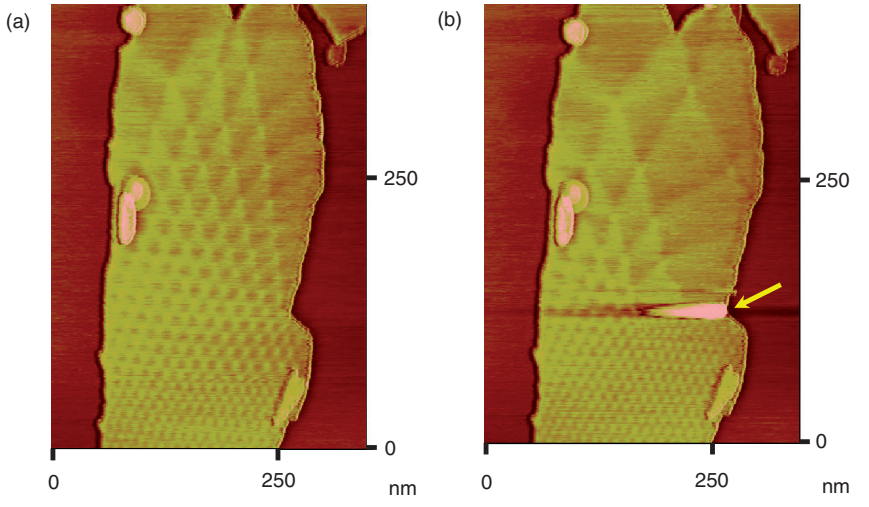

Figure 9. STM images of the superperiodic pattern on a necktie-shaped nanographene sheet on a HOPG substrate (a) before and (b) after a nanographene flake is placed on it. The observations are carried out at the bias voltage of $V = 200\,\mathrm{mV}$ and the current of $I = 0.7\,\mathrm{nA}$. The arrow in (b) denotes the position where the nanographene flake is placed [46].

necktie and the HOPG substrate is over 0.8 nm, suggesting that it consists of a stacking of two nanographene sheets, which interact weakly with the HOPG substrate. A unique superperiodic pattern is observed on the nanographene sheet. Interestingly, the period and the amplitude of the oscillations decrease from the top to the bottom along the longitudinal direction of the nanographene necktie. The oscillation period is one order of magnitude larger than that of the Moiré pattern due to stacking [64] and therefore this possibility can be excluded. The oscillation period becomes longer and shorter by placing a nanographene flake on the nanographene necktie in the upper and lower regions from the flake, respectively, as shown in figure 9(b). Indeed, the oscillation period becomes doubled in the upper region of the necktie after addition of the flake. The oscillation below the flake seems to be only slightly modified by the flake. Such an effect on the oscillations cannot be explained by some structural modulations, but is an effect due to the interference of the electronic wavefunctions confined on the nanographene surface. It should be noted that the nanographene sheet inclines along its longitudinal direction with its top higher than the bottom with a slope of $\Delta z/\Delta y \sim 2 \times 10^{-4}$, according to the observation of the line profile, where the x, y and z directions are defined as the long and short directions on the nanographene sheet, and the direction perpendicular to the sheet, respectively. This suggests that the inclination of the nanographene sheet should be responsible for the change of the periodicity in the superperiodic pattern along the y-direction.

Here, the observed superperiodic pattern is theoretically understood as the interference phenomenon of the π-electrons on the basis of the $k \cdot p$ method, in which the kinetic energy of the graphitic π-electron has a linear k-dependence [48]. By assuming a static electric potential $-Fy$ which is proportional to the y-axis coordinate, and a confinement effect due to the well-shaped potential within $-d/2 < x < d/2$ (d is

the width of the nanographene along the x-direction), the Hamiltonian around the K-point with the linear potential $-Fy$ is given as [65, 66]

$$H = \begin{pmatrix} -Fy & -i\gamma\dfrac{\partial}{\partial x} - \gamma\dfrac{\partial}{\partial y} \\ -i\gamma\dfrac{\partial}{\partial x} + \gamma\dfrac{\partial}{\partial y} & -Fy \end{pmatrix}, \tag{2}$$

where $\gamma \equiv (\sqrt{3}/2)a\gamma_0$, a is the bond length of the C–C bond in a graphene sheet, and γ_0 is the intra-sheet transfer integral [48] for the nearest neighbour carbon atoms. This model is solved with a well potential $V_{\text{well}}(x)$ having an infinite depth. The Schrödinger equation $H\Psi = E\Psi$ gives an oscillatory solution as given by the following equation:

$$\Psi = 2A \begin{pmatrix} \sin\left(\dfrac{E_n x}{\gamma}\right) \sin\left[\dfrac{1}{\gamma}\left(\tilde{E}y + \dfrac{1}{2}Fy^2\right)\right] \\ -i\cos\left(\dfrac{E_n x}{\gamma}\right) \cos\left[\dfrac{1}{\gamma}\left(\tilde{E}y + \dfrac{1}{2}Fy^2\right)\right] \end{pmatrix}, \tag{3}$$

where $E_n = n\pi\gamma/d$ and $\tilde{E} = E - E_n$. The electron density at the A-sublattice point is calculated as

$$|\psi_A(\boldsymbol{R}_A)|^2 = 4A^2 \sin^2\left(\frac{n\pi x}{d}\right)\left\{1 + \cos[(\boldsymbol{K} - \boldsymbol{K}') \cdot \boldsymbol{R}_A] \sin\left[\frac{2}{\gamma}\left(\tilde{E}y + \frac{1}{2}Fy^2\right)\right]\right\} \tag{4}$$

where $\boldsymbol{R}_{\text{A}}$ is the lattice point of the A sublattice, $\boldsymbol{K}$ and $\boldsymbol{K}'$ are the K- and K'-points in the wavenumber space. We pay particular attention to the long-period oscillating component:

$$\sin^2\left(\frac{n\pi x}{d}\right)\left[\text{constant} + \sin\left(\frac{Fy^2}{\gamma} - \frac{2n\pi}{d}y\right)\right], \tag{5}$$

where $E = 0$ is taken at the Fermi energy. This functional form for the quantum number $n = 4$ is plotted in figure 10 with the assumption of $d = 1$. The amplitude is spatially constant, and the oscillation period becomes smaller as y becomes larger. This result of the theoretical calculation can well reproduce the observed decrease of the oscillation period shown in figure 9, although a uniform array for the standing wave would be the result of the simplified theory and this is in contrast with the observations.

The observed peak positions of the electron density along the y-direction are plotted in figure 11 in comparison with the theoretical results of equation (5) and of the free electron model. The slight decrease found in the experiments cannot be reproduced by the theoretical result from the $k \cdot p$ model, even though the decrease of the oscillation period is in fair agreement with the experimental results. The fitting gives a parameter of the potential gradient of $F = 6.49 \times 10^{-3}\,\text{eV nm}^{-1}$. The total potential variation over the distance 200 nm becomes 1.3 eV. Such a magnitude of the potential change can survive against thermal lattice fluctuations and the superperiodic pattern can really exist

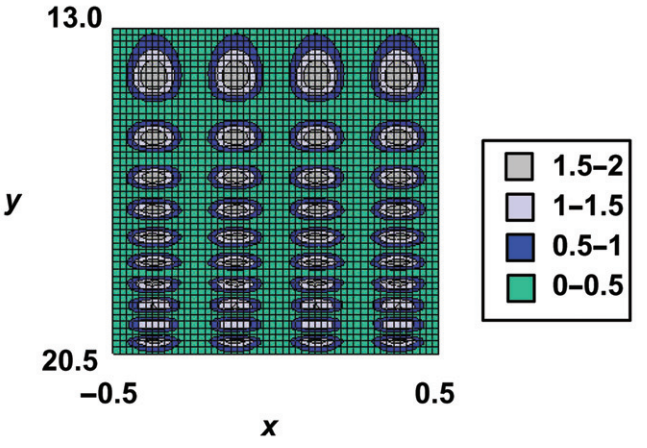

Figure 10. A 2D plot of the electron density calculated using the $k{\cdot}p$ method. The horizontal and vertical axes are shown in arbitrary units. The quantum number 4 is taken for the standing wave within the infinite well; $-0.5 < x < 0.5$ with $d = 1$. The numbers in the square box on the right denote the contour of the electron density (arbitrary units) [46].

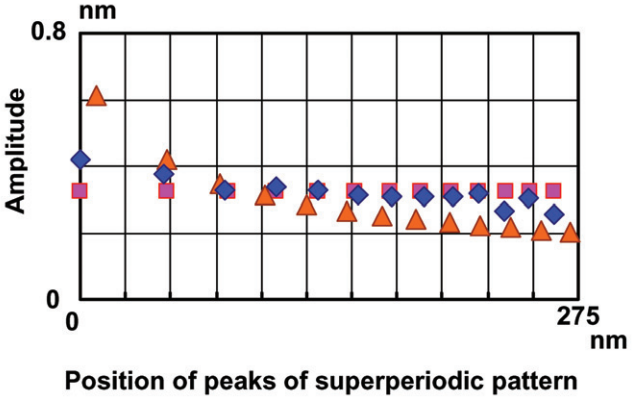

Figure 11. Comparison of plots of the amplitude *vs* peak position (parallel to the *y*-direction) in the electron wave superperiodic patterns from the STM image (diamond), the free electron model (triangle), and the $k \cdot p$ model (square) [46].

in experiments. It should be noted that a similar analysis with the free electron model gives the potential gradient three orders of magnitude smaller than that obtained by the $k \cdot p$ model and is less than the thermal lattice fluctuations. This indicates the importance of the k-linear energy dispersion of the π-electrons in the interference phenomenon that is observed.

4.2. *Interference at the interface between graphene sheets and the substrate*

Interference phenomena can happen also in the direction perpendicular to the graphene sheet [47]. This is related to the interference in the graphene sheets interacting at the

interface with the substrate. Heat-treatment at ca.1600°C makes the surface of a HOPG flake degraded, resulting in the creation of an interface between the HOPG flake and a few graphene sheets that come off from the former. At the same time, dislocations are created at the interface by the heat-treatment [47]. Figure 12 presents an STM image for one of the typical examples showing a dislocation network pattern generated at the interface. There is a step edge which divides the observed region into the upper right and lower left subregions. According to the STM observation of the line profile, the lower terrace in the lower left subregion has a thickness of two graphene sheets (0.67 ± 0.2 nm), while the upper terrace in the upper right subregion has a thickness of three sheets (0.39–0.41 nm above the lower terrace). The superperiodic pattern observed clearly in figure 12(a) is associated with the dislocation network created in the interface as observed in previous works of STM [67, 68] and TEM [69–71] experiments. The diffraction pattern of the dislocation network is attributed to the modified local density of states (LDOS) caused by rhombohedral stacking faults due to partial dislocations. The partial dislocations are defined by the Burgers vector that converts an *AB*-stacked sheet in ordinary graphite to an *AC*-stacked sheet with respect to a glide plane. The conversion of stacking occurs abruptly accompanied with a lattice distortion where a sharp-edged periodic pattern is generated. Interestingly, the superperiodic pattern on the lower terrace is continuously connected to that on the upper terrace with no effect of the step edge.

In figure 12(a), three regions are indicated; regions A, B, and C contain a triangular-shaped pattern, a rhombic-shaped pattern, and a net-shaped pattern, respectively. In the intermediate regions A–B and B–C, there are complicated contrasts that are superimposed of the patterns in the two regions. In regions A and B, the apparent height of lines which divide the patterns into individual geometric units is lower than the centre of the unit by about 0.1 nm. Crossed points of lines are further depressed from the lines by about 0.1 nm, resulting in the 'contracted nodes' in the image. In region C, however, lines are imaged higher than the centre of the unit by about 0.05 nm and crossed points of the lines are the highest (about 0.005 nm higher than the lines), giving the 'extended nodes' in the image. Except for the slight contrast, the patterns in regions B and C appear to have contrast inverted from each other. Figure 12(b) is a magnified image near a contracted node of the upper terrace in figure 12(a), which is marked by a black dot, taken at $V_s = 0.002$ V, $I = 1.7$ nA. A straight line drawn on triangular lattice points at the bottom right part is extended to the valley sites of the triangular lattice at the top left part, indicating the presence of a distortion at the centre part of the image. This atomically resolved image supports the identification that the observed patterns come from the dislocation-network structure. As for patterns at higher bias voltages, figures 13(a)–(c) display images of almost the same places as figure 12(a) at bias voltages of 0.3, 0.4, and 0.5 V, respectively. For clarity, the dependence of the height differences between two points on the upper and lower terraces on the bias voltage are shown in figure 13(d). Just by increasing the bias voltage, the patterns on the upper terrace in figure 13(a) are changed from a triangle-shaped pattern into a net-shaped one which is similar to that on the lower terrace in figure 13(c). The net-shaped pattern on the lower terrace remains unchanged not so obviously upon the

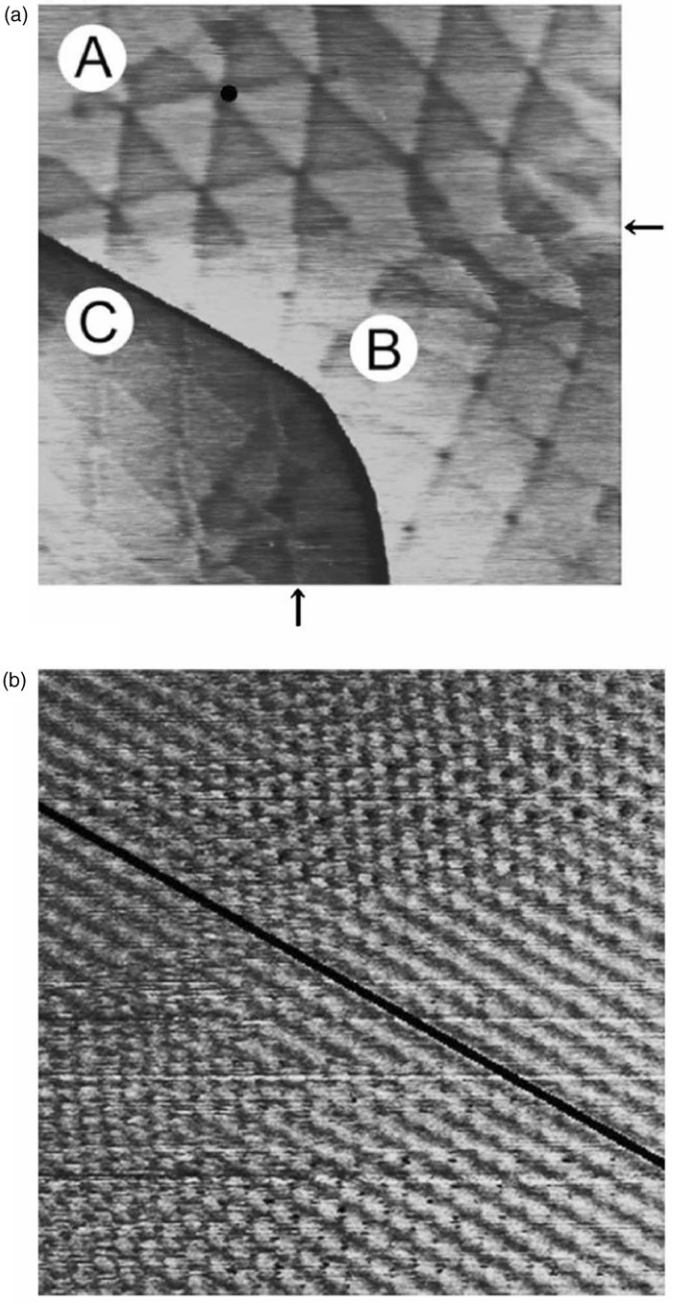

Figure 12. (a) STM image ($500 \times 500\,nm^2$) of the superperiodic patterns at a low sample bias voltage of 0.02 V, which are expected to reflect the density of states close to the Fermi level. A, B, and C denote the regions of triangular-, rhombic-, and net-shaped patterns, respectively. Arrows indicate complicated patterns, where two patterns are superimposed. Lines that divide the geometric patterns into individual units cross at contracted nodes in regions A and B, and at extended nodes in region C. (b) Atomically resolved STM image ($6.0 \times 6.0\,nm^2$) of one individual triangular pattern near a contracted node on the upper terrace in (a), which is marked by a black dot, at $V_s = 0.002$ V and $I = 1.7$ nA. A straight line placed on triangular lattice sites at the bottom right part is extended to the valley sites of the triangular lattice at the top left part through a distorted lattice part [47].

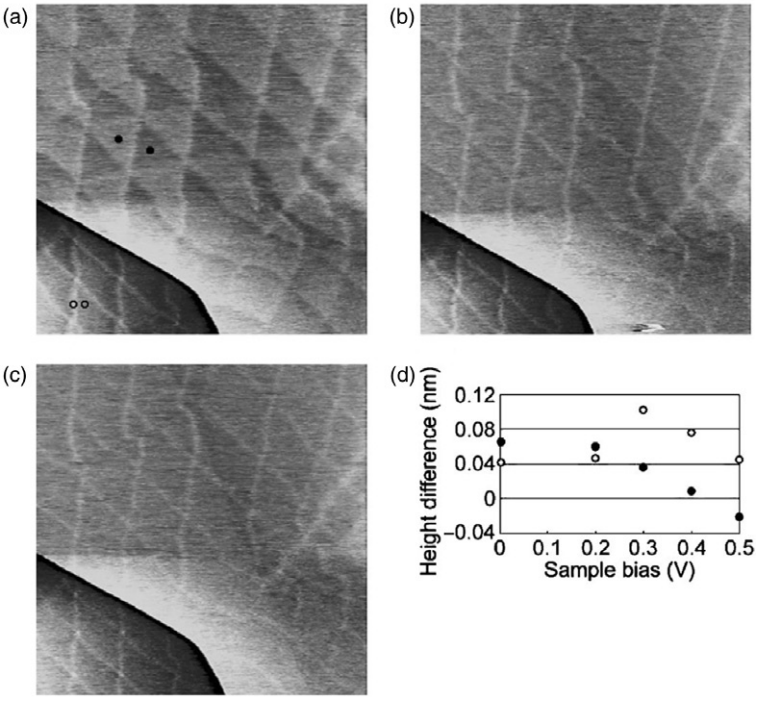

Figure 13. STM images ($500 \times 500\,nm^2$) of superperiodic patterns at sample bias voltages; (a) $V_s = 0.3\,V$, (b) $V_s = 0.4\,V$, and (c) $V_s = 0.5\,V$. By increasing the bias voltage, the corrugation amplitude of superperiodic patterns on the upper terrace (upper right) decreases gradually [(a) and (b)] and change into a net pattern (c). In contrast, no significant change is observed for the pattern on the lower terrace (lower left). The net pattern appearing on the upper terrace of (c) is similar to that on the lower terrace. Height differences between two points depicted in (a) are shown in (d) for clarifying the bias-dependent contrast. Solid and blank circles are the height differences of the upper and lower terraces, respectively. Circles at the sample bias of around 0 V are the height differences at $V_s = 0.02\,V$ [47].

elevation of the bias voltage, as shown in figures 13(a)–(c). Changes of corrugation amplitudes with a maximum at $V_s = 0.3\,V$ are observed in the patterns on the lower terrace as shown in figure 13(d).

The experimental results shown in figures 12 and 13 demonstrate that the superperiodic corrugation amplitudes of the observed patterns vary without any change in the periodicity, depending on the overlayer height from the substrate and the bias voltage of the STM. The continuity of the pattern at the step edge indicates that the patterns observed on both terraces come from the same origin; that is, the dislocation network at the interface that is extended over the wide region including the step edge, since an array of faulted stacking is not changed abruptly across the step edge. Here, it should be noted that the experimental results cannot be explained merely by calculating the density of states of faulted stacking, because the observed patterns at different terraces have contrasts inverted from each other as shown in figures 12 and 13. We also cannot explain the property, on

the basis of the faulted stacking, that the superperiodic corrugation amplitudes on the lower terrace become larger although the gap between the tip and the sample becomes larger when increasing the bias voltage from 0.02 to 0.3 V as shown in figure 13(d). In other words, the observed behaviour is considered to be due to the LDOS at the surface, taking into account the fact that the observed corrugation amplitudes become larger. Then, the LDOS should explain the gradual decreases of the corrugation amplitudes and the variations of patterns on the upper terrace in increasing the bias voltage without changing the periodicity of the patterns, and that should also explain the increase of the corrugation amplitudes on the lower terrace when increasing the bias voltage near the Fermi energy.

Here, we discuss the interference effect for explaining the bias-voltage dependence of superperiodic patterns on the basis of a theoretical treatment reported in [64]. Considering the scattering potential at the interface, one can find that the LDOS at the surface is related to the interference effect of the electrons that are scattered at the surface and the interface between the overlayer and the substrate. The LDOS at the surface can be given as $\sin^2(kz)$ using coordinate z and a wavenumber k along the axis normal to the surface (the z-axis) in the case that the lateral wavenumber of a superperiodic pattern is nearly equal to 0 by comparison with the wavenumber originating from the lattice. If one treats the scattering potential at the interface by a perturbation, a beat can be generated by the interference between the perturbed and the unperturbed waves. In this case, the LDOS at the surface is proportional to $\sin(kz)\cos(k'z)$, where k' and k are a perturbed wavenumber and an unperturbed wavenumber, respectively.

Let us take a square-patterned potential with a periodicity of $2L$ at the interface as shown in figure 14 for simplicity, in analysing theoretically the superperiodic pattern, which is related to the probability density of the wavefunction confined in the plane with a periodic abrupt potential change associated with the dislocation network [47]. We place a square potential with $L/3$ in width and $4v_0\delta(z)$ in height, where L is the half of the periodicity of the square potential and v_0 is the strength of the scattering potential, at the line dividing the patterns into geometrical units. Though the square-shaped pattern in the present model is different from the experimental result (the rhombus-shaped pattern in regions B and C, triangular-shaped pattern in region A), it can make a theoretical treatment easier with any loss of validity. If we locate the surface and the interface positions at l and 0, respectively, in the z-axis as shown in figure 14(c) and introduce a delta function $\delta(z)$ at the interface, this potential can be expressed using the Fourier analysis

$$V(x,y,z) = \left(\hbar^2/m_\perp\right)\upsilon_0 \sum_n a_n \delta(z)\left(e^{iq_{xn}x} + e^{-iq_{xn}x} + e^{iq_{yn}y} + e^{-iq_{yn}y}\right), \tag{6}$$

where $m_\perp$ is the effective mass along the z axis, a_n is the nth component which equals $\{2/(n\pi)\}\{\sin(n\pi) - \sin(5n\pi/6)\}$ for the square potential, and q_{xn} and q_{yn}, which take discrete values $(n\pi/L)(n = 1, 2, \ldots)$, are the components of the nth wavevectors in the x- and y-axes, respectively. Assuming the linear combination of in-plane plane

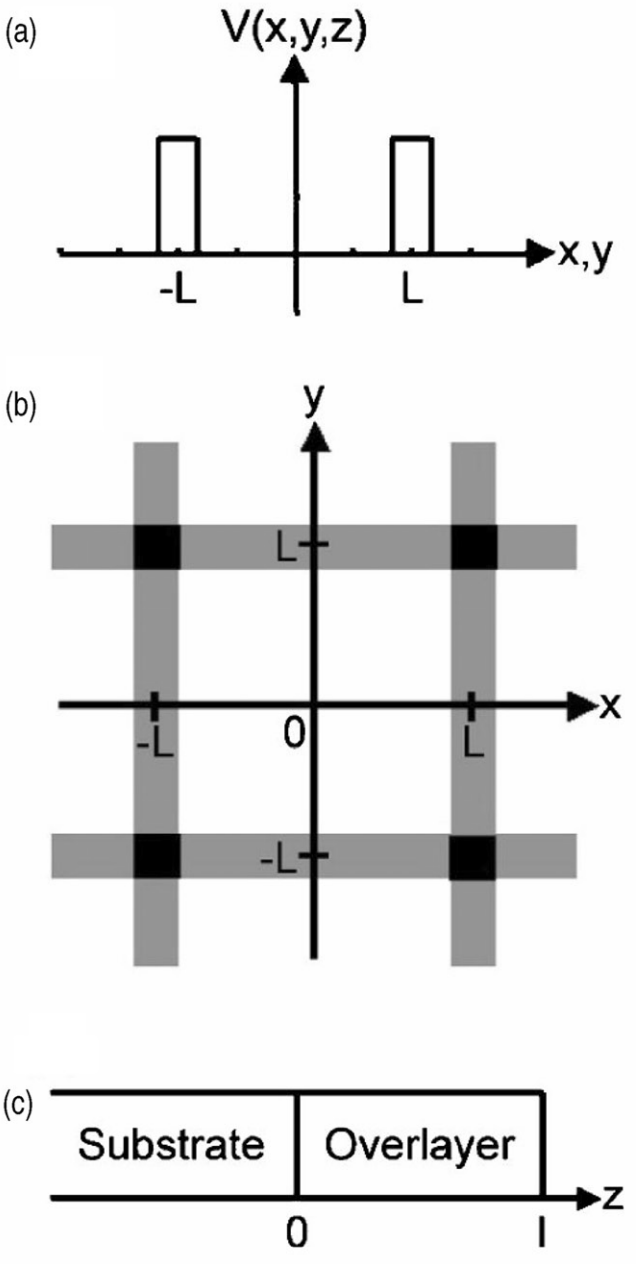

Figure 14. Model of the potential at the interface between the graphene overlayer and the HOPG substrate. (a) The cross-sectional profile of square potential along the x- and y-axes. The periodicity is $2L$ and the potential is $(1/3)L$ in width and $2v_0\delta(x)$ in height. (b) The projection of the square-patterned potential on the xy plane. Grey lines represent potential lines and black squares represent potential nodes, whose potential height is the sum of the 1D potentials in x- and y-axes. The height of the potential nodes is twice as large as that of the potential lines. (c) The position of the surface and the interface along the z-axis. The surface and the interface are located at l and 0 in the z axis, respectively [47].

waves and wavefunctions $A_{qxqy}(z)$ for the z component, the wavefunction is represented to be

$$\Psi(x,y,z) = \sum_{q_x,q_y} A_{q_x,q_y}(z) e^{i(q_x x + q_y y)}. \tag{7}$$

Based on this wavefunction and the connecting condition derived from the Schrödinger equation with the square patterned potential, the perturbed wavefunction is given as

$$\Psi^{\pm}(x,y,z) = \upsilon_0 \sum_n [a_n/(ik')]\left(1 - e^{2ikl}\right)\left(e^{ik'z} - e^{ik'z+2ik'l}\right) \times e^{\pm i(q_{xn}\cdot x + q_{yn}\cdot y)}. \tag{8}$$

where the term of v_0^2 is neglected because of its small contribution. For the unperturbed wave, we take a plane wave in the direction of the z axis,

$$\Psi_0 = e^{ikz}, \quad k'^2 = k^2 - \left(m_{||}/m_{\perp}\right)\left|\mathbf{q}_n\right|^2 \tag{9}$$

where $m_{||}$ is the effective mass in the xy plane. Since the total wavefunction $\Psi_{total}(x, y, z)$ is the sum of Ψ^+, Ψ^-, and Ψ_0, the probability density around the surface, $|\Psi_{total}(x, y, z)|^2$, is roughly expressed with an overlayer height from the substrate, l, the perturbed wavenumber, k', and the unperturbed wavenumber, k [47]:

$$\left|\Psi_{total}(x,y,z)\right|^2 = -\lambda \sum_n a_n k \sin(kl)\cos(k'l) \times \left\{\cos(q_{xn}\cdot x) + \cos\left(q_{yn}\cdot y\right)\right\} + \text{const}, \tag{10}$$

where λ and the second term are positive constants, and the second term has a larger absolute value than the first term. In this equation, the spatially varied probability density, which gives a superperiodic pattern, corresponds to the term $\{\cos(q_{xn}\ x) + \cos(q_{yn}y)\}$. By attributing the unperturbed wave to the wavefunction in bulk graphite, the energy dispersion can be given using parameter $m_{\perp}$, the interlayer distance c, and the interlayer resonance integral, γ_1 (=0.39 eV) [72]:

$$E = \frac{\hbar^2 k^2}{(2m_{\perp})} - 2\gamma_1, \quad m_{\perp} = \frac{\hbar^2}{(2c^2\gamma_1)}. \tag{11}$$

The investigation of the spatially varied LDOS is important in order to look over the contrast image of the STM from the corrugation amplitude of a superperiodic pattern that depends on a bias voltage. In this connection, the difference of the LDOS at the surface, $\{|\Psi_{total}(0,0,0)|^2 - |\Psi_{total}(L,0,0)|^2\}$, where the former and latter terms represent the LDOS at the centre and the edge of an individual geometric pattern unit, respectively, can give a simple diagnosis in mapping a superperiodic pattern because the potential height is constant except for the edge part with a fine oscillation originating from the Fourier analysis.

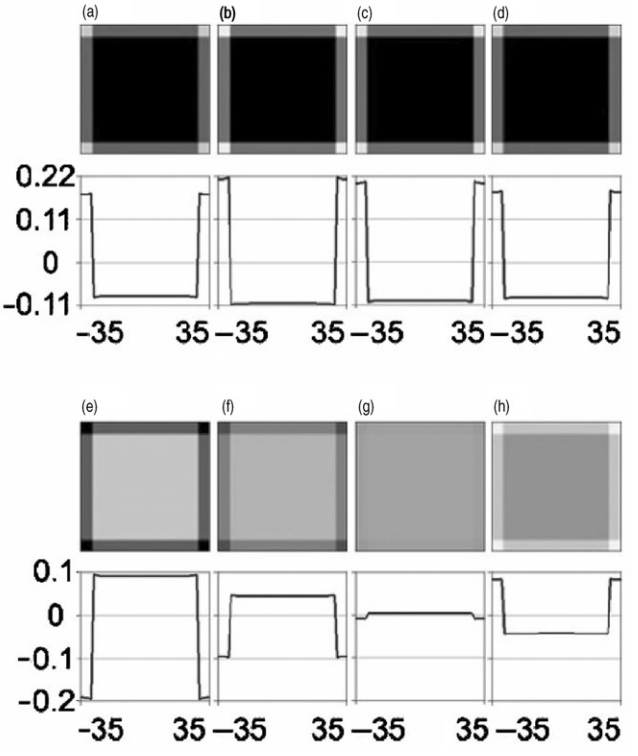

Figure 15. The calculated LDOS in a $2L \times 2L$ square (upper) and its cross-sectional profile passing through the centre of the geometrical unit (lower) at different overlayer heights and bias voltages: (a) $l = 1.5$ (layer), $V_s = 0.02$ V, (b) $l = 1.5$, $V_s = 0.30$, (c) $l = 1.5$, $V_s = 0.40$, (d) $l = 1.5$, $V_s = 0.50$ V, (e) $l = 2.7$, $V_s = 0.02$ V, (f) $l = 2.7$, $V_s = 0.30$ V, (g) $l = 2.7$, $V_s = 0.40$ V, and (h) $l = 2.7$, $V_s = 0.50$ V. (Top pictures) Lighter brightness indicates a higher LDOS value. (Bottom pictures) The x or y value in the lateral axis (unit : nm), the LDOS in the vertical axis (arbitrary units). The number of sheets in the graphene overlayer is given as $s = 2$ and 3 for $l = 1.5$ and 2.7, respectively, after correction [47].

Figure 15 shows the calculated LDOS in a $2L \times 2L$ square of the individual geometrical pattern unit at different graphene overlayer heights and varied bias voltages. The extended and contracted nodes appear at the crossing points $(x, y) = (\pm L, \pm L)$, $(\pm L, \pm L)$. At $l = 1.5$ (number of sheets $s = 2$), the difference of the LDOS is enhanced with increasing the bias voltage from 0.02 to 0.3 V, where the calculated superperiodic patterns are net-shaped patterns with the extended nodes as clearly seen in figures 15(a)–(d). This result is in excellent agreement with the experimental evidence that the inverted superperiodic patterns (net-shaped patterns) are observed on the lower terrace (two graphene sheets high from the substrate) near the step edge, as shown in figures 12 and 13. Indeed, the increase of the corrugation amplitude in figures 12(a) and 13(a) can be understood on the basis of the increased difference of the LDOS because the corrugation amplitude is roughly proportional to the LDOS, as mentioned above. At $l = 2.7$ ($s = 3$), the difference of the LDOS decreases in increasing the bias voltage from 0.02 to 0.40 V, where the calculated superperiodic patterns become square-shaped patterns with contracted nodes as shown in figures 15(e)–(g), although the pattern shape

(square shaped) is different from that of the experimental results (rhombic and triangular shaped). By further increase in the bias voltage (0.4 to 0.5 V), the difference of the LDOS has a negative value with a net-shaped pattern with extended nodes in figure 15(h). This result supports the experimental evidence that the corrugation amplitude of the superperiodic pattern on the higher terrace (three graphene sheets high from the substrate) decreases gradually and that the superperiodic pattern changes into an inverted pattern with increasing the bias voltage further, as shown in figure 13. Eventually, the observed superperiodic patterns can be explained by the dislocation network at the interface and an interference in the graphene overlayer dependent on its thickness and bias voltages.

5. Edge state in nanographene

According to the theoretical work mentioned in Section 2, the electronic structure of nanographene depends on the shape of the edges. Around zigzag edges, we have a non-bonding π-electron state (edge-state), in spite of the absence of such a state in armchair edges [13–16]. The localized spins of the edge states have been revealed to show unconventional nanomagnetism as well from theoretical and experimental approaches [23–38]. In the meantime, it is of particular importance to confirm experimentally the presence of the edge state and to clarify the correlation between the edge structure of graphene sheets and the electronic feature of the edge state. STM/STS observations are the most powerful tool for this purpose. Along this line of experimental works with STM/STS, early investigations have been carried out with graphene sheets in the ambient atmosphere [73–75]. Here, it should be noted that the graphite samples handled in the ambient atmosphere have edges bonded to various oxygen-including functional groups due to the oxidation of the edges or chemical species introduced in the sample preparation process. The presence of various kinds of functional groups at the edges modifies the electronic structure of the edge state depending on the electronic features of these functional groups. Therefore, the employment of well defined edges is particularly important to clarify the correlation between the edge structure and the electronic feature of the edge state. In this sense, the hydrogen-terminated graphene edges give us well defined edges which can be compared with the theoretical results. Recent STM/STS works of well defined hydrogen-terminated edges have revealed interesting electronic features of the edge state which depend on the detailed structures of the edges. In this section, the experimental results are reviewed on the STM/STS observations carried out under ultra-high vacuum (UHV) conditions with hydrogen-terminated graphene edges [44, 45], which show clear STM images of zigzag and armchair edges of graphene near the Fermi level, and STS curves in order to clarify the relationship between the edge structure and the distribution of edge states.

As for STM/STS observations under UHV conditions ($\sim 5 \times 10^{-11}$ torr), the HOPG samples were heated at ca. 800°C to eliminate functional groups including oxygen in the form of CO [76] immediately followed by exposure to atomic hydrogen to terminate the edges of graphite in a UHV sample treatment chamber directly connected to the STM observation chamber. The conditions for the hydrogenation of the edges were the same as those for hydrogenation of the Si(100) surface to make a monohydride surface [77].

Adsorbed contaminants on the edges and graphite surface can be removed by reaction with pure hydrogen during the hydrogenation process. By several repeats of the heat treatments and hydrogenation in the preparation chamber, the structure of the edges is arranged due to the removal of hydrocarbons from hydrogen-terminated edges [78, 79]. The STM/STS measurements were carried out at room temperature.

The dispersion relation and 2D LDOS mapping were calculated using the tight-binding approximation for *AB*-stacked double-sheet graphene. The first sheet represents the top graphene sheet with edges and the second sheet represents the graphite substrate. The resonance integral and the overlap integral were parametrized using the Slater–Koster parameters [80] and were determined for the 2*s* and 2*p* orbitals of carbon and the 1*s* orbital of hydrogen. The structural dependence of the parameters was determined following [81]. For carbon–hydrogen bonding, the parameters of hydrogen were fitted to reproduce the band structure of graphene strips with zigzag edges obtained by a first-principles calculation with the local density approximation [82, 83]. Several percentages of the displacements of carbon atoms near each edge were neglected in the Hückel approximation. This makes the calculation tractable without harming essential features in the density of states.

5.1. *Edge state and the electronic structure of the graphene edges*

The experimental results prove that zigzag edges are much shorter in length than armchair edges and less frequently observed. This suggests that the structure of a zigzag edge is energetically more unstable than that of an armchair edge, in good agreement with theoretical results showing that the stability of an armchair edge is higher than that of a zigzag edge in terms of the total energy [13, 84, 85]. A typical atomically-resolved UHV STM image of hydrogenated graphene edge line that comprises of short zigzag and armchair edge parts is shown in figure 16(a), in which the upper part is a zigzag edge with armchair edges being in the centre and bottom parts. Figure 17 allows us to understand the geometrical relation between armchair edges and zigzag edges. Figure 16(a) clearly shows that the LDOS distribution is dependent on the edge structures, which can be observed only for the samples with the edges hydrogen-terminated under the UHV condition. The microscopy image at a low bias voltage proves that the edge states are observed as bright spots at a homogeneous zigzag edge, but they are not at armchair edges distant from zigzag edges. The observed image, including the $(\sqrt{3} \times \sqrt{3})R30^\circ$ superlattice, of homogeneous zigzag and armchair edges can be reproduced using the calculated data in [74]. The image of armchair edges in figure 16(a) is not homogeneous because the armchair edges are perturbed by the adjacent zigzag edge and corner points. The STS data of figure 16(b) clearly verify the presence of the edge states at the zigzag edge. In the figure, one peak at ca. -0.03 V corresponds to the density-of-states peak of the edge states, which are assigned to the flat band near the Fermi level suggested in the theory in [15, 16]. Taking the rapid decay of the LDOS (the brightness of the bright spots) from the edge to the interior of the graphene sheet into consideration, the flat band of the edge states is associated mainly with the $k = \pi$ state at the Brillouin zone boundary, because the LDOS for the $k = 2\pi/3$ state oscillates and does not decay [15, 16]. The origin of another peak at 0.2 V in figure 16(b) is attributed to charge transfer from the zigzag edge to physisorbed atoms

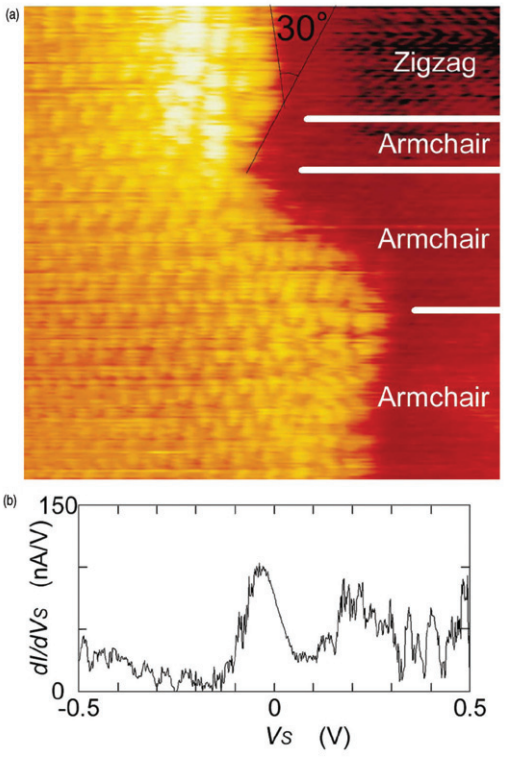

Figure 16. (a) An atomically-resolved UHV STM image of zigzag and armchair edges ($9 \times 9\,\mathrm{nm}^2$) observed in constant-height mode with bias voltage $V_s = 0.02\,\mathrm{V}$ and current $I = 0.7\,\mathrm{nA}$. (b) The $\mathrm{d}I/\mathrm{d}V_s$ curve from STS data at a zigzag edge [44].

or molecules. Taking into account the facts that the hydrogenation process and the subsequent STS observation are not completely free of impurity species and that the obtained STS data include few changes in relative position between the tip and the sample due to the thermal drift, this interpretation is reasonable [73].

Figure 18(a) show atomically resolved UHV STM images of a part of long homogeneous armchair edge line with edge carbon atoms completely hydrogenated. This clearly indicates the absence of bright spots associated with edge states around the armchair edge. In addition, the density of states obtained by the $\mathrm{d}I/\mathrm{d}V_S$ curve at the armchair edge of figure 18(a) can be described only in terms of linear π- and π^*-bands with no contribution of the edge-state peak at the Fermi energy as shown in figure 18(b). Here, the π- and π^*-bands correspond to the contributions below and above $V_s = 0\,\mathrm{V}$, respectively, in the figure. These facts firmly demonstrate that the edge states are not observed on the homogeneous armchair edge, in good agreement with what the theory predicts [15, 16].

In contrast to the image of the homogeneous armchair edge, that of defective armchair edges is obviously different as shown in figure 19(a). The defects in the image consist of the sites from which four extra rows of carbon atoms are added to the lower part of the armchair edge, as understood from the honeycomb lattice drawn in figures 19(a). In other words, it is a partial zigzag edge of four edge carbon atoms

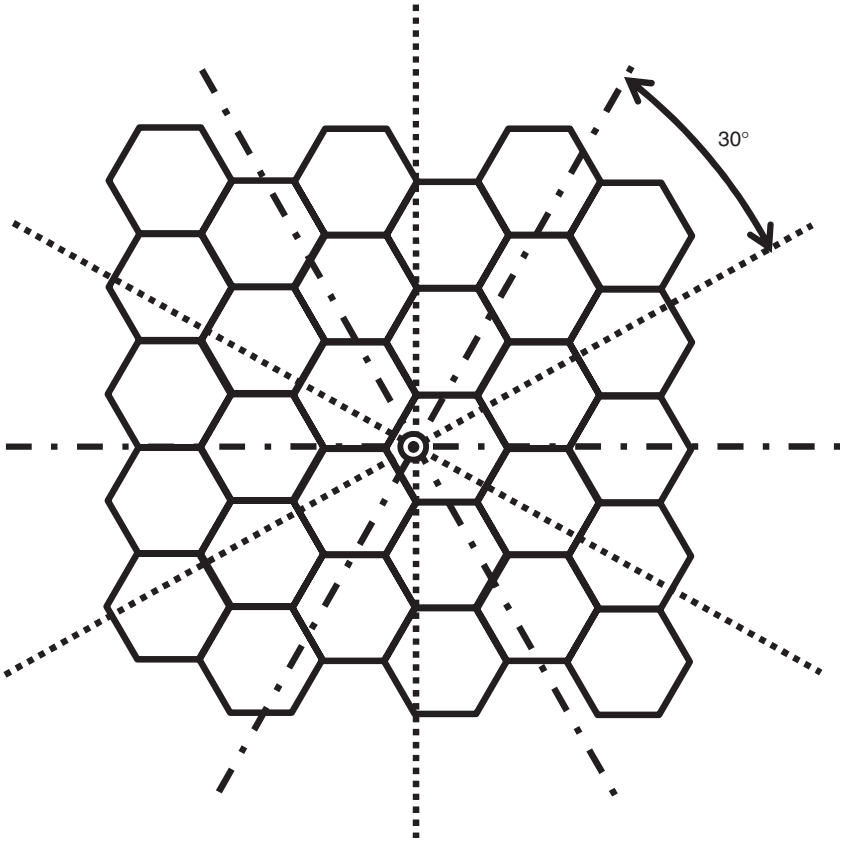

Figure 17. Schematic model of zigzag and armchair edges that are made by cutting along dotted and dash-dotted lines, respectively. Zigzag and armchair edges alternately appear by rotating a cut line by every 30°.

embedded in the armchair edges. The origin of the bright points in figures 19(a) is understood by looking at the LDOS of the defect points of the armchair edges. Figure 19(b) shows the 2D mapping of the LDOS of the defect structure which is the same as that observed in figure 19(a). The tight-binding approximation for *AB*-stacked double-sheet graphene is applied for the analysis. From the calculated result, the centre of the distribution of the relatively large LDOS corresponds to the partial zigzag edge embedded between the armchair edges. Figure 19(b) shows a localized inclination of edge electrons and it well reproduces isolated bright points, which are observed in figure 19(a), at the partial zigzag edge. The figure also reproduces the $(\sqrt{3} \times \sqrt{3})R30^\circ$ superlattice near the defect points.

5.2. *Effects of intersheet interaction, structural modification of the edge, and electron confinement on the electronic features of the edge states*

The features of the edge states vary depending on several factors, such as imperfection of the edge structure, defects, intersheet interaction, structural modification of the

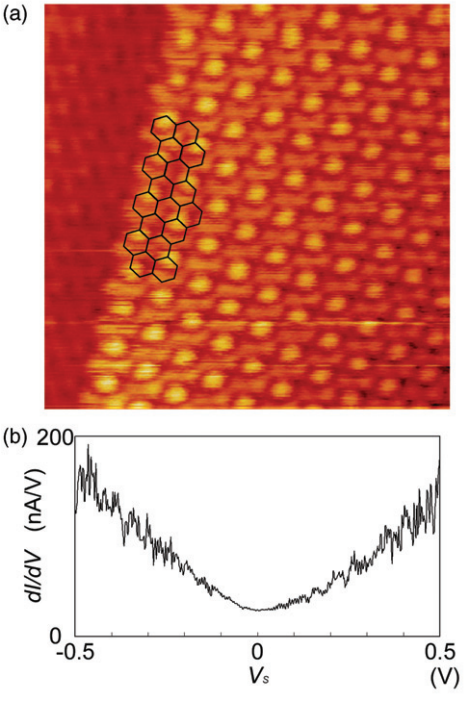

Figure 18. (a) Atomically resolved UHV STM images ($5.6 \times 5.6\,nm^2$) of a homogeneous armchair edge in constant-height mode with bias voltage $V_s = 0.02\,V$ and current $I = 0.7\,nA$. For clarity of edge structures, a model of the honeycomb lattice is drawn on the image. (b) A dI/dV_s curve from STS measurements taken at the edge in (a) [44].

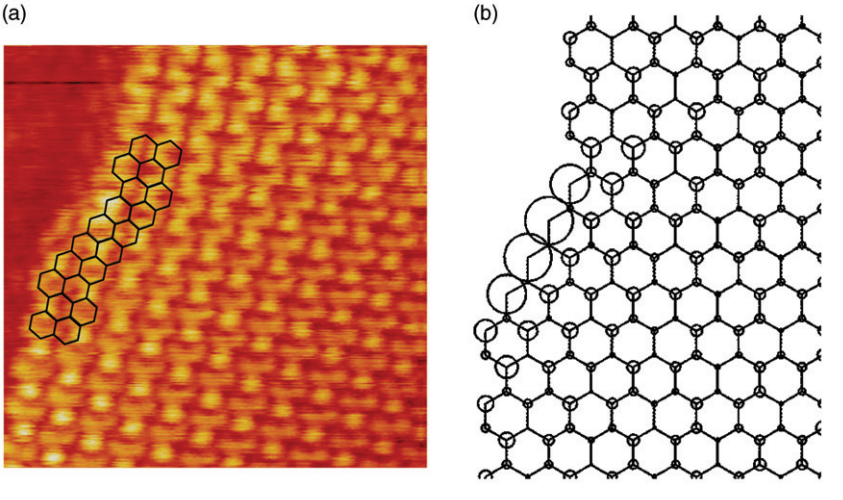

Figure 19. (a) Atomically resolved UHV STM images ($5.6 \times 5.6\,nm^2$) of an armchair edge with defect points. The defect consists of a partial zigzag edge having four edge carbon atoms embedded in the armchair edges. (b) 2D mappings of the LDOS that reproduce the observed STM images of (a) using a tight-binding approximation for *AB*-stacked double-sheet graphene. The dimension of the circle on each lattice point denotes the relative value of the LDOS that is accumulated in the range of 50 meV near the Fermi level [44].

zigzag edges, electron confinement effect, etc. We have already suggested the effects of the imperfection and defects in the last section. As we discussed in Section 3.1, the intersheet interaction, whose strength ($\gamma_1 = 0.39$ eV) is about one order of magnitude smaller than that of the intra-sheet interaction ($\gamma_0 = 3.16$ eV) [48]. Therefore, the intersheet interaction is expected to contribute to modifying the electronic feature of the edge state. Structural modifications of the edges are also important in the change of the edge states, according to theoretical suggestion. Indeed, Klein and Kusakabe prove that the distribution of the LDOS is strongly modified by adding extra π-conjugated carbon atoms bonded to the edge carbon atoms at the zigzag edge [21–24]. In the meantime, finite-length zigzag edges or armchair edges are affected by the adjacent armchair or zigzag edges. Electron confinement effects in a finite system and state mixing between zigzag and armchair edges are among the important phenomena appearing in finite size systems. Here, we discuss the variety of the electronic structures of the edge states as shown above.

The first example is the intersheet interaction affecting the feature of the edge state. Figure 20 presents a typical image observed at an edge whose mean direction runs along a zigzag direction of the top graphene sheet. By applying the relationship shown in figure 17 to the image of figure 20, we can assign the parts of the edge to armchair or zigzag. In figure 20, there are two types of partial zigzag edges termed 'Z1' and 'Z2', whose directions are tilted by 60° and 0° with respect to the mean edge direction, respectively. There are some differences in the observed distributions of bright spots between the 'Z1' and 'Z2' zigzag edges. The edge carbon atoms of the 'Z1' edge are

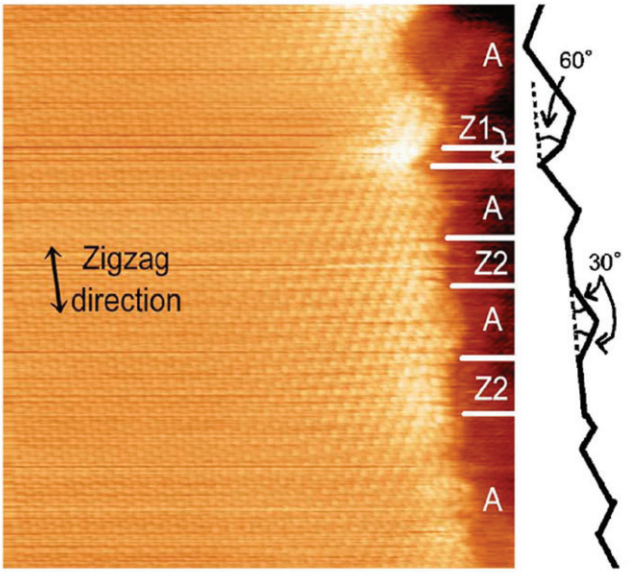

Figure 20. STM image ($14.8 \times 13.4\,nm^2$) of a graphene edge that runs in the zigzag direction. The edge consists of a combination of zigzag and armchair edges. Labels 'Z1' and 'Z2' denote partial zigzag edges that run in different directions, and label 'A' denotes a partial armchair edge. The contour of the edge is drawn in parallel to the edge for clarifying positions and angles of the partial zigzag and armchair edges [45].

brighter than those of the 'Z2' edge. In addition to this, the bright spots of the 'Z1' edge are limited only to the vicinity of the edge carbon atoms and their neighbouring sites, whereas the bright spots of the 'Z2' edge are extended to the interior of the sheet.

The origin of the difference in the distributions of the observed bright spots can be understood by the schematic model in figure 21(a), in which the stacking nature of graphite is taken into account, and two types of zigzag edges are connected with each other with an angle of 60°. The geometric relation in figure 21(a) is constructed to extract the relation of the 'Z1' and 'Z2' edges in figure 20. The relation in figure 21(a) indicates that the edge carbon atoms at the top right and the bottom correspond to α- and β-site carbon atoms, respectively. For the calculation of the LDOS to be compared with the experimental result in figure 20, a model is constructed as shown in figure 21(b). In this model, the two types of zigzag edges have the same geometrical relation as that in figure 21(a), except that the presence of an armchair edge between the two zigzag edges decreases the overlap of the edge states between the two types of zigzag edges. In figure 22, the LDOS at each α-site (β-site) carbon atom in the rectangles in figure 21(b) is plotted as a function of the position of the α-site (β-site) carbon atom from the α-site (β-site) edge carbon atom to the interior of the graphene sheet. The LDOS shows a decay from the edge to the interior with an oscillation that comes from a superperiodic pattern near the edges. Figure 22 reveals a clear difference in the LDOS distributions at the partial zigzag edges terminated by the α- and β-site carbon atoms. The magnitudes of the LDOS of the edge carbon atoms at α sites are larger than those at β sites. The LDOS whose edge carbon atoms are assigned to the α site decays rapidly to the interior of the sheet, whereas that of the β sites decays slowly. In other words, the LDOS is more localized at the zigzag edge of α sites, in contrast to the extended feature in that of β sites. These results qualitatively reproduce the distribution of the bright spots in figure 20. With this excellent agreement of the characters between the observed and calculated results, the edge carbon atoms of the 'Z1' and the 'Z2' edges correspond to the α- and β-site carbon atoms, respectively.

The modifications of graphene edges also change the electronic feature of the edge state. The simplest modification can be made by changing a monohyrogenated edge carbon atom to a dihydrogenated one by adding an extra hydrogen atom to the edge carbon atom. This change reminds us of the difference between a monohydrogenated zigzag edge (Fujita edge) and a Klein edge. Figure 23 presents an example of this modification; the STM image shows an armchair edge with a defect from which two rows of extra carbon atoms are added to the lower region of the armchair edge. An array of bright spots, whose brightness decreases monotonically toward the interior of the sheet along a line with an angle of 120° from the direction of the armchair edge, is observed near the defect point in figure 23. The image is compared to the spatial distribution of the LDOS calculated by the tight-binding method with the same geometry as that of the lattice experimentally observed, as shown in figure 24(a). A comparison demonstrates that the LDOS mapping fails to reproduce the direction of the array of bright spots in the observed STM image. Indeed, the array of the calculated LDOS runs along a line with an angle of 60° from the direction of the armchair edge, in disagreement with that observed.

Here, we note the difference in the stacking structures, which is an excellent explanation for the case of figure 20. However, the difference between the stacking

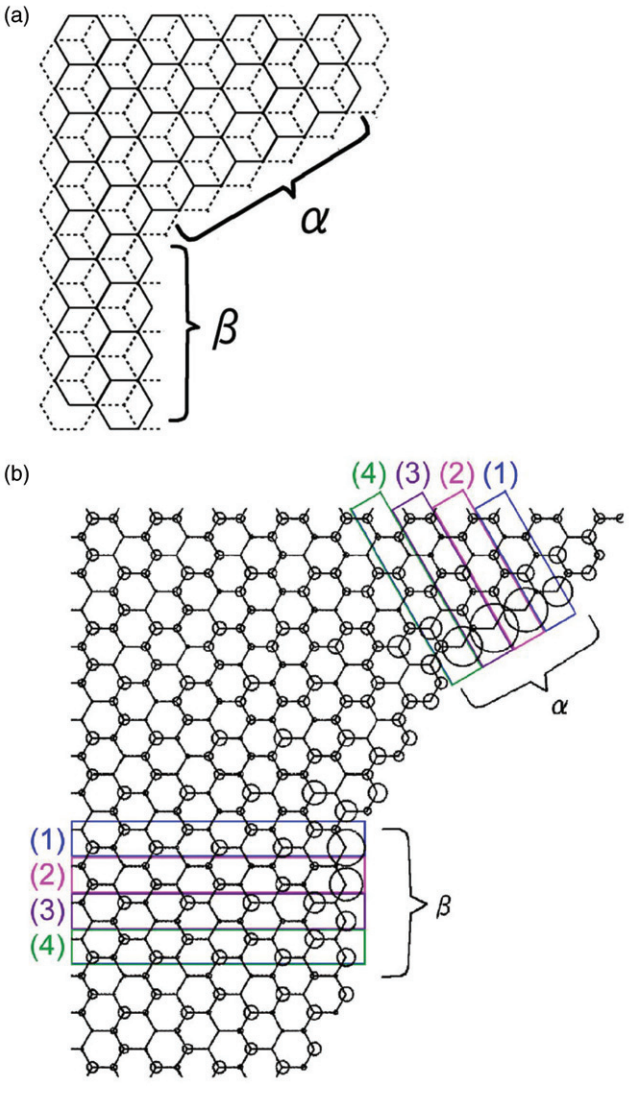

Figure 21. (a) Schematic model of *AB*-stacked double-sheet graphene that forms two types of zigzag edges whose edge carbon atoms belong to α or β sites. The angle between the two types of zigzag edges is 60°. Honeycomb lattices drawn by solid and dotted lines represent the top and second sheets, respectively. (b) 2D mapping of the LDOS of a graphene sheet having interconnected two partial zigzag edges whose directions differ by 60° from each other. They are separated with an armchair edge region to avoid interference between the edge states of the two partial zigzag edges. Each zigzag edge in the model consists of four edge carbon atoms. The α-site (β-site) edge carbon atoms of partial zigzag edges exist at top right (bottom) part. The LDOS of α-site and β-site carbon atoms in the rectangles are plotted in figure 22 [45].

structures, that is, the difference of α or β site at the defect point or the difference between *AA* and *AB* stackings, is not a candidate for the origin of this disagreement, because the observed difference cannot be reproduced on the basis of the calculations with the difference of the α or β site. The difference that originates from the local

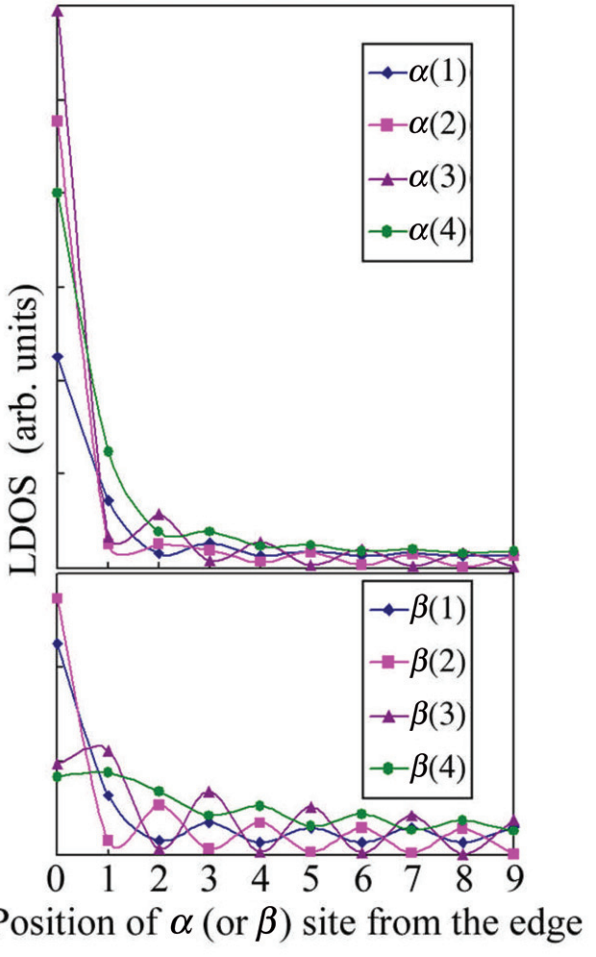

Figure 22. Plots of the LDOS in the rectangles numbered in figure 21(b) as a function of α-site (β-site) carbon atoms from the α-site (β-site) edge carbon atoms to the interior of the sheet. Solid lines are the guides for the eyes [45].

stacking structure can create only a difference in the magnitudes of the LDOS like in the case of figure 21(b) and do not give any difference in the direction of an array with a relatively large LDOS. Hence, the origin of the difference in the direction of the array of bright spots may come from the difference in the detailed edge carbon structure that cannot be clearly distinguished by the STM observation. The origin of the difference may be associated with the presence of an extra carbon atom that is bonded to the edge carbon atom in the sample preparation process, for example. The smallest structural difference at the defect point can be made by the presence or absence of extra one carbon atom bonded to the edge carbon atom; that is, the presence or absence of a Klein edge at the defect. Figure 24(b) is the calculated result based on the model that has the same geometric structure as that of figure 24(a) except that an extra carbon atom is attached to the partial zigzag edge. Figure 24(b) well reproduces the array of

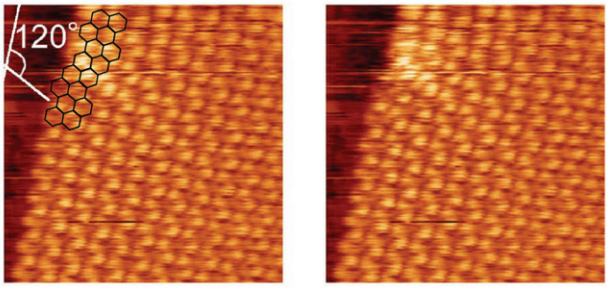

Figure 23. STM image ($4.5 \times 4.5\,nm^2$) of an armchair edge with a defect from which two rows of carbon atoms are added to the lower region of the armchair edge. In the left panel, a honeycomb lattice is overlaid on the original image in the right panel for clarifying the location of the defect. An array of bright spots is observed at around the defect point, and its direction and the angle measured from the direction of the armchair edge is drawn in the left panel [45].

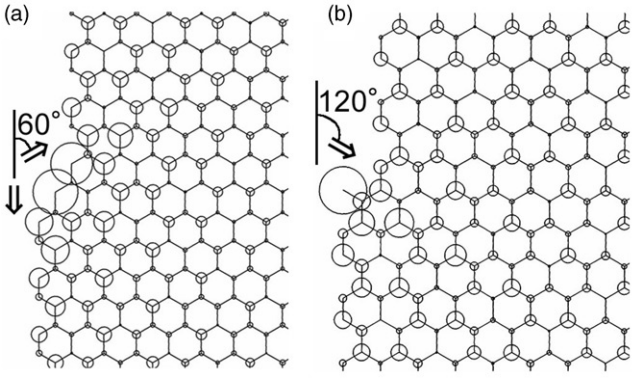

Figure 24. (a) 2D mapping of the LDOS at the defect point of the armchair edge, which corresponds to the image in figure 23. (b) 2D mapping of the LDOS of the edge structure same as (a) except that an extra carbon atom, which is drawn as a bar, is attached to an edge carbon atom of the partial zigzag edge. Arrows indicate the direction of the array of large LDOS (bright spots) [45].

bright spots in figure 23. The direction of an array of the LDOS of figure 24(b) is 120° from the direction of the armchair edge and is changed by 60° from that of figure 24(a) by the presence of a Klein edge.

The final discussion is devoted to the electron confinement effect in a finite length zigzag edge. Figure 25(a) shows an STM image of a zigzag edge which consists of seven edge carbon atoms. In this image, the bright spot that represents the edge state is absent at the centre of the zigzag edge, although bright spots at other edge carbon atoms in the zigzag edge prove the presence of the edge state. The absence of bright spots is always detected in a zigzag edge that is longer than that in figure 25(a). In the calculated result in figure 25(b) of the zigzag edge structure similar to that in the observed edge, the LDOS at the centre part of the partial zigzag edge is very small although the atomic structure does not have any vacancy in the edge. This is because the smallest LDOS in the edges corresponds to the node of the wavefunction of an electron that is confined in the finite length zigzag edge having an odd number of edge carbon atoms.

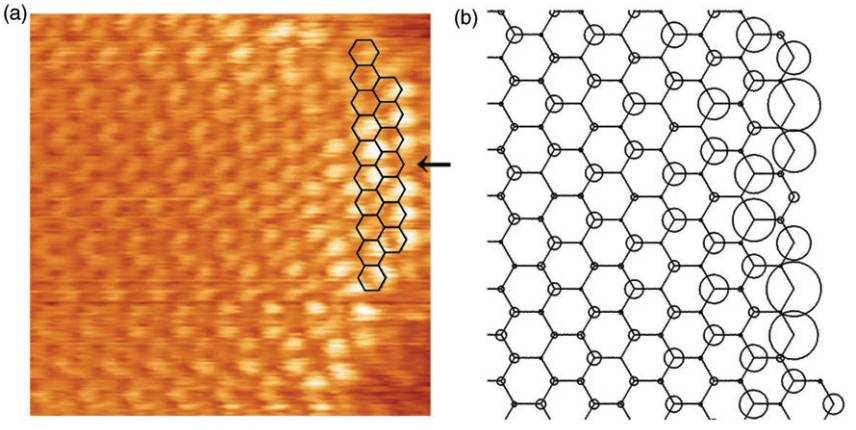

Figure 25. (a) STM image ($3.8 \times 3.8\,nm^2$) of a zigzag edge consisting of seven edge carbon atoms. The arrow indicates a very small LDOS at the centre of the zigzag edge. (b) 2D mapping of the LDOS at a zigzag edge whose structure is the same as that in (a) [45].

6. Conclusion

Nanographene, which is a nanosized system of graphene, is one of the important partners in π-electron-based nanocarbon family, in which fullerenes, carbon nanotubes and graphene are involved. In contrast to fullerenes, carbon nanotubes and graphene, which have a closed π-electron system with no edges or have a minor contribution of the edges, nanographene has the electronic structure of an open π-electron system due to the presence of open edges. The circumference of an arbitrary-shaped nanographene is described in terms of a combination of zigzag and armchair edges. Theoretical investigations demonstrate the formation of a non-bonding π -state (edge state) at a zigzag edge, in spite of the absence of such a state in an armchair edge. The edge state is relevant to the non-bonding π-state appearing at the Fermi level in non-Kekulé-type condensed polycyclic aromatic hydrocarbon molecules. The edge states are localized around the edge carbon atoms in the zigzag edge, giving localized spins. Therefore, the edge state is of particular interest from the point of producing carbon-only molecular magnetism in nanosystems. Indeed, according to theoretical and experimental works, ferromagnetism can be created in the edge-state spins in nanographene ribbons having modified zigzag edges.

Nanographene can be prepared by heat-induced conversion of nanodiamond particles on a HOPG substrate, on which the particles are seeded in a controlled manner using an electrophoretic technique. Nanographene ribbons are found by chance around step edges of graphite. Individual nanographene ribbons can be structurally characterized by a combination of AFM and resonance Raman spectroscopy.

The finiteness in size of nanographene brings about interference phenomena of the wavefunction due to the electron confinement effect. A nanographene sheet inclined along a direction is found to show an interference superperiodic pattern with a varying periodicity. The stacking of sheets also gives an interference effect on the dislocation network created by rhombohedral stacking faults.

Microprobe techniques of STM/STS provide a powerful tool for investigating the correlation between the electronic and structural features of nanographene edges at atomic resolution, when the edges are well defined by hydrogenation of edge carbon atoms. The experimental observations demonstrate that armchair edges are generally long and defect free, whereas zigzag edges tend to be short and defective. This proves that the zigzag edges which have non-bonding edge states at the Fermi level are energetically unstable in comparison with armchair edges, in good agreement with theoretical prediction. STM/STS experiments confirms the presence of edge states well localized around the edge carbon atoms in zigzag edges, while no edge state appears in armchair edges. The features of the edge states depend on the detailed structure of edges. The edge state in a short zigzag edge embedded between armchair edges is affected by state mixing which makes the LDOS of the edge state extended toward the interior of the nanographene sheet. The edge state in a short length zigzag edge is subjected to the electron confinement effect, showing a node of the wavefunction at the centre of the zigzag edge. It is also affected by the intersheet interaction. Indeed, the spatial distribution of the LDOS of the edge state varies depending on the geometry of the site in the sheet stacking between α- and β-sites.

Nanographene having a desirable shape is obtained theoretically by cutting a graphene sheet along the direction which is intentionally determined. In addition, chemical modifications of edge carbon atoms vary the electronic and magnetic features of edge states. For example, monohyrogenation of the edge carbon atoms in a zigzag edge gives itinerant magnetism, while dihydorgenation brings about localized features in the magnetism. Fluorination makes magnetism disappear. The termination of edge carbon atoms with oxygen atoms makes zigzag edges electrically conductive. The future development of electron lithography with atomic resolution in combination with chemical modifications is expected to give well defined edges having a variety of electronic and magnetic functions. Nanographene is more easily tailored than fullerenes and carbon nanotubes. In this sense, nanographene is a future promising target material in the development of molecular spintronics/electronics devices in nanotechnology.

Acknowledgements

The authors express their sincere thanks to Kouichi Kusakabe, Kikuo Harigaya, and Katunori Wakayayashi for fruitful discussion. The present work was supported by Grant-in-Aid for Scientific Research No. 15105005 from the Ministry of Education, Culture, Sports, Science, and Technology, Japan.

References

[1] M.S. Dresselhaus, G. Dresselhaus, and P.C. Eklund, *Science of Fullerenes and Carbon Nanotubes* (Academic Press, San Diego, 1996).
[2] R. Saito, G. Dresselhaus, and M. S. Dresselhaus, *Physical Properties of Carbon Nanotubes* (Imperial College Press, London, 1998).

[3] Y. Zheng and T. Ando, Phys. Rev. **B65,** 245420 (2002).
[4] K. S. Novoselov, A. K. Geim, S. V. Morozov, D. Jiang, Y. Zhang, S. V. Dubonos, I. V. Grigorieva, and A. A. Firsov, Science **306,** 666 (2004).
[5] K. S. Novoselov, A. K. Geim, S. V. Morozov, D. Jiang, M. I. Katsnelson, I. V. Grigorieva, S. V. Dubonos, and A. A. Firsov, Nature **438,** 197 (2005).
[6] Y. Zhang, Y.-W. Tan, H. L. Stormer, and P. Kim, Nature **438,** 201 (2005).
[7] C. L. Kane and E. J. Mele, Phys. Rev. Lett. **95,** 226801 (2005).
[8] T. Ohta, A. Bostwich, T. Seyller, K. Horn, and E. Rotenberg, Science **313,** 951 (2006).
[9] Y. Zhang, Z. Jiang, J. P. Small, M. S. Purewal, Y.-W. Tan, M. Fazlollahi, J. D. Chudow, J. A. Jaszczak, H. L. Stomer, and P. Kim, Phys. Rev. Lett. **96,** 136806 (2006).
[10] K. S. Novoselov, Z. Jiang, Y. Zhang, S. V. Morozov, H. L. Stormer, U. Zeitler, J. C. Maan, G. S. Boebinger, P. Kim, and A. K. Geim, Science **315,** 1379 (2007).
[11] J. C. Meyer, A. K. Geim, M. I. Katsnelson, K. S. Novoselov, T. J. Booth, and S. Roth, Nature **446,** 60 (2007).
[12] P. G. Silvestrov and K. B. Efetov, Phys. Rev. Lett. **98,** 0106802 (2007).
[13] S. E. Stein and R. L. Brown, J. Am. Chem. Soc. **109,** 3721 (1987).
[14] K. Yoshizawa, K. Okahara, T. Sato, K. Tanaka, and T. Yamabe, Carbon **32,** 1517 (1994).
[15] M. Fujita, K. Wakabayashi, K. Nakada, and K. Kusakabe, J. Phys. Soc. Jpn. **65,** 1920 (1996).
[16] K. Nakada, M. Fujita, G. Dresselhaus, and M. Dresselhaus, Phys. Rev. **B54,** 17954 (1996).
[17] K. Wakabayashi, M. Fujita, H. Ajiki, and M. Sigrist, Phys. Rev. **B59,** 8271 (1999).
[18] M. Kastler, J. Schmidt, W. Pisula, D. Sebastiani, and K. Müllen, J. Amer. Chem. Soc. **128,** 9526 (2006).
[19] D. Jiang, B. G. Sumpter, and S. Dai, J. Chem. Phys. **126,** 134701 (2007).
[20] K. Wakabayashi, Y. Takane, and M. Sigrist, Phys. Rev. Lett. **99,** 036601 (2007).
[21] D. J. Klein, Chem. Phys. Lett. **217,** 261 (1994).
[22] D. J. Klein and L. Bytautas, J. Phys. Chem. **A 103,** 5196 (1999).
[23] K. Kusakabe and M. Maruyama, Phys. Rev. **B67,** 092406 (R) (2003).
[24] M. Maruyama and K. Kusakabe, J. Phys. Soc. Jpn. **73,** 656 (2004).
[25] Y.-W. Son, M. L. Cohen, and G. Louie, Nature **444,** 347 (2006).
[26] T. Enoki and Y. Kobayashi, J. Mater. Chem. **15,** 3999 (2005).
[27] T. Enoki and K. Takai, Carbon-Based Magnetism: An Overview of the Magnetism of Metal Free Carbon-Based Compounds and Materials, F. Palacio and T. Makorova, eds., Elsevier Science, 397 (2006).
[28] Y. Shibayama, H. Sato, T. Enoki, X. X. Bi, M. S. Dresselhaus, and M. Endo, J. Phys. Soc. Jpn. **69,** 754 (2000).
[29] Y. Shibayama, H. Sato, T. Enoki, and M. Endo, Phys. Rev. Lett. **84,** 1744 (2000).
[30] P. Esquinazi, A. Setzer, R. Höhne, C. Semmelhack, Y. Kopelevich, D. Spemann, T. Butz, B. Kohlstrunk, and M. Lösche, Phys. Rev. **B66,** 024429 (2002).
[31] P. Esquinazi, D. Spemann, R. Höhne, A. Setzer, K.-H. Han, and T. Butz, Phys. Rev. Lett. **91,** 227201 (2003).
[32] P. O. Lehtinen, A. S. Foster, Y. Ma, A. V. Krasheninnikov, and R. M. Nieminen, Phys. Rev. Lett. **93,** 187202 (2004).
[33] A. W. Mombrú, H. Pardo, R. Faccio, O. F. de Lima, E. R. Leite, G. Zanelatto, A. J. C. Lanfredi, C. A. Cardoso, and F. M. Araújo-Moreira, Phys. Rev. **B71,** 100404(R) (2005).
[34] H. Sato, N. Kawatsu, T. Enoki, M. Endo, R. Kobori, S. Maruyama, and K. Kaneko, Solid State Commun. **125,** 641 (2003).
[35] K. Harigaya and T. Enoki, Chem. Phys. Lett. **351,** 128 (2002).
[36] H. Sato, N. Kawatsu, T. Enoki, M. Endo, R. Kobori, S. Maruyama, and K. Kaneko, Carbon **45,** 214 (2006).
[37] A. Nakayama, K. Suzuki, T. Enoki, C. Ishii, K. Kaneko, M. Endo, and N. Shindo, Solid State Commun. **93,** 323 (1995).
[38] K. Sugihara, A. Nakayama, and T. Enoki, J. Phys. Soc. Jpn. **64,** 2614 (1995).
[39] Y. Li, S. Xie, W. Zhou, D. Tang, X.-P. Zou, Z. Liu, and G. Wang, Carbon **39,** 626 (2000).
[40] A. M. Affoune, B. L. V. Prasad, H. Sato, and T. Enoki, Langmuir **17,** 547 (2001).
[41] A. M. Affoune, B. L. V. Prasad, H. Sato, T. Enoki, Y. Kaburagi, and Y. Hishiyama, Chem. Phys, Lett. **348,** 17 (2001).
[42] M. Naito, M. Kitada, S. Nishigaki, and N. Toyoda, Surf. Rev. Lett. **10,** 473 (2003).
[43] L. G. Cançado, M. A. Pimenta, B. R. A. Neves, G. Medeiros-Ribeiro, T. Enoki, Y. Kobayashi, K. Takai, K. Fukui, M. S. Dresselhaus, R. Saito, and A. Jorio, Phys. Rev. Lett. **93,** 047403 (2004).
[44] Y. Kobayashi, K. Fukui, T. Enoki, K. Kusakabe, and Y. Kaburagi, Phys. Rev. **B71,** 193406 (2005).
[45] Y. Kobayashi, K. Fukui, T. Enoki, and K. Kusakabe, Phys. Rev. **B73,** 125415 (2006).
[46] K. Harigaya, Y. Kobayashi, K. Takai, J. Ravier, and T. Enoki, J. Phys.: Condens. Mat. **14,** L605 (2002).

[47] Y. Kobayashi, K. Takai, K. Fukui, T. Enoki, K. Harigaya, Y. Kaburagi, and Y. Hishiyama, Phys. Rev. **B69,** 035418 (2004).
[48] B. T. Kelly, *Physics of Graphite* (Applied Science Publishers, London, 1981).
[49] K. Goto, T. Kubo, K. Yamamoto, K. Nakasuji, K. Sato, D. Shiomi, T. Takui, T. Kobayashi, K. Yakushi, and J. Qutang, J. Amer. Chem. Soc. **121,** 1619 (1999).
[50] K. Fukui, K. Sato, D. Shiomi, T. Takui, K. Itoh, K. Gotoh, T. Kubo, K. Yamamoto, K. Nakasuji, and A. Naito, Synth. Metals **103,** 2257 (1999).
[51] E. H. Lieb, Phys. Rev. Lett. **62,** 1201 (1989).
[52] J. Inoue, K. Fukui, D. Shiomi, Y. Morita, K. Yamamoto, K. Nakasuji, T. Takui, and K. Yamaguchi, J. Amer. Chem. Soc. **123,** 12702 (2001).
[53] O. E. Andersson, B. L. V. Prasad, H. Sato, T. Enoki, Y. Hishiyama, Y. Kaburagi, M. Yoshikawa, and S. Bandow, Phys. Rev. **B58,** 16387 (1998).
[54] B. L. V. Prasad, H. Sato, T. Enoki, Y. Hishiyama, Y. Kaburagi, A. M. Rao, P. C. Eklund, K. Oshida, and M. Endo, Phys. Rev. **B62,** 11209 (2000).
[55] H. Nagayoshi, Band Theory of Graphite; A New Method for Layer-Type Crystals. PhD thesis, University of Tokyo, Tokyo, Japan, 1975.
[56] A. Gruneis, R. Saito, Ge. G. Samsomidze, T. Kimura, M. A. Pimenta, A. Jorio, A. G. Souza Filho, G. Dresselhaus, and M. S. Dresselhaus, Phys. Rev. **B67,** 165402 (2003).
[57] Y. Miyamoto, K. Nakada, and M. Fujita, Phys. Rev. **B59,** 9858 (1999).
[58] F. L. Shyu, M. F. Lin, C. P. Chang, R. B. Chen, J. S. Shyu, Y. C. Wang, and C. H. Liao, J. Phys. Soc. Jpn. **70,** 3348 (2001).
[59] M. F. Lin and F. L. Shyu, J. Phys. Soc. Jpn. **69,** 3529 (2000).
[60] C. W. Chiu, F. L. Shyu, C. P. Chang, R. B. Chen, and M. F. Lin, J. Phys. Soc. Jpn. **72,** 170 (2003).
[61] P.-H. Tan, Y.-M. Deng, Q. Zhao, and W.-C. Cheng, Appl. Phys. Lett. **74,** 1818 (1999).
[62] H. Herchen and M. A. Cappelli, Phys. Rev. **B43,** 11740 (1991).
[63] E. S. Zouboulis and M. Grimsditch, Phys. Rev. **B43,** 12490 (1991).
[64] K. Kobayashi, Phys. Rev. **B53,** 11091 (1996).
[65] H. Ajiki and T. Ando, J. Phys. Soc. Jpn. **62,** 1255 (1993).
[66] T. Ando and T. Nakanishi, J. Phys. Soc. Jpn. **67,** 1704 (1998).
[67] J. Xhie, K. Sattler, M. Ge, and N. Venkateswaran, Phys. Rev. **B47,** 15835 (1993).
[68] Z. Y. Rong and P. Kuiper, Phys. Rev. **B48,** 17427 (1993).
[69] P. Delavignette and S. J. Amelinckx, Nucl. Mater. **5,** 17 (1962).
[70] G. K. Williamson, Proc. R. Soc. London **A 257,** 457 (1960).
[71] S. R. Snyder, T. Foecke, H. S. White, and W. W. Gerberich, J. Mater. Res. **7,** 341 (1992).
[72] N. A. W. Holzwarth, S. G. Louie, and S. Rabii, Phys. Rev. **B26,** 5382 (1982).
[73] Z. Klusek, Z. Waqar, E. Denisov, T. Kompaniets, I. Makarenko, A. Titkov, and A. Bhatti, Appl. Surf. Sci. **161,** 508 (2000).
[74] P. Giunta and S. Kelly, J. Chem. Phys. **114,** 1807 (2001).
[75] Y. Niimi, T. Matsui, H. Kambara, K. Tagami, M. Tsukada, and H. Fukuyama, Appl. Surf. Sci. **241,** 43 (2005).
[76] K. Moriguchi, S. Munetoh, M. Abe, M. Yonemura, K. Kamei, A. Shintani, and Y. Maehara, J. Appl. Phys. **88,** 6369 (2000).
[77] J. Boland, Surf. Sci. **261,** 17 (1992).
[78] T. Zecho, A. Güttler, and J. Küppers, Carbon **42,** 609 (2004).
[79] T. Zecho, A. Güttler, X. Sha, B. Jackson, and J. Küppers, J. Chem. Phys. **117,** 8486 (2002).
[80] J. C. Slater and G. Koster, Phys. Rev. **94,** 1498 (1954).
[81] D. Papaconstantopoulos, M. Mehl, S. Erwin, and M. Pederson, in *Tight-Binding Approach to Computational Materials Science*, edited by P. E. A. Turchi, A. Gonis, and L. Colombo, MRS Symposia Proceedings No. 491 (Materials Research Society, Pittsburgh, 1998), p. 221.
[82] J. P. Perdew and Y. Wang, Phys. Rev. **B45,** 13 (1992).
[83] J. Yamauchi, M. Tsukada, S. Watanabe, and O. Sugino, Phys. Rev. **B54,** 5586 (1996).
[84] Y. H. Lee, S. G. Kim, and D. Tománek, Phys. Rev. Lett. **78,** 2393 (1997).
[85] T. Kawai, Y. Miyamoto, O. Sugino, and Y. Koga, Phys. Rev. **B62,** R16349 (2000).